

CHORUS IV: Mapping the Spatially Inhomogeneous Cosmic Reionization with Subaru HSC

TAKEHIRO YOSHIOKA,¹ NOBUNARI KASHIKAWA,^{1,2} AKIO K. INOUE,^{3,4} SATOSHI YAMANAKA,⁵ KAZUHIRO SHIMASAKU,^{1,2}
YUICHI HARIKANE,^{6,7} TAKATOSHI SHIBUYA,⁸ RIEKO MOMOSE,⁹ KEI ITO,^{10,11,1} YONGMING LIANG,^{10,11,1} RIKAKO ISHIMOTO,¹
YOSHIHIRO TAKEDA,¹ MASAMI OUCHI,^{12,13,14} AND CHIEN-HSIU LEE¹⁵

¹*Department of Astronomy, School of Science, The University of Tokyo, 7-3-1 Hongo, Bunkyo-ku, Tokyo, 113-0033, Japan*

²*Research Center for the Early Universe, The University of Tokyo, 7-3-1 Hongo, Bunkyo-ku, Tokyo 113-0033, Japan*

³*Department of Physics, School of Advanced Science and Engineering, Faculty of Science and Engineering, Waseda University, 3-4-1 Okubo, Shinjuku, Tokyo 169-8555, Japan*

⁴*Waseda Research Institute for Science and Engineering, Faculty of Science and Engineering, Waseda University, 3-4-1 Okubo, Shinjuku, Tokyo 169-8555, Japan*

⁵*General Education Department, National Institute of Technology, Toba College, 1-1, Ikegami-cho, Toba, Mie 517-8501, Japan*

⁶*Institute for Cosmic Ray Research, The University of Tokyo, 5-1-5 Kashiwanoha, Kashiwa, Chiba 277-8582, Japan*

⁷*Department of Physics and Astronomy, University College London, Gower Street, London WC1E 6BT, UK*

⁸*Kitami Institute of Technology, 165 Koen-cho, Kitami, Hokkaido 090-8507, Japan*

⁹*Kavli IPMU (WPI), UTIAS, The University of Tokyo, Kashiwa, Chiba 277-8583, Japan*

¹⁰*Department of Astronomical Science, The Graduate University for Advanced Studies, SOKENDAI, Mitaka, Tokyo, 181-8588, Japan*

¹¹*National Astronomical Observatory of Japan, Mitaka, Tokyo, 181-8588, Japan*

¹²*National Astronomical Observatory of Japan, Osawa 2-21-1, Mitaka, Tokyo 181-8588, Japan*

¹³*Institute for Cosmic Ray Research, The University of Tokyo, Kashiwanoha 5-1-5, Kashiwa, Chiba 277-8582, Japan*

¹⁴*Kavli Institute for the Physics and Mathematics of the Universe (Kavli IPMU, WPI), The University of Tokyo, Kashiwanoha 5-1-5, Kashiwa, Chiba 277-8583, Japan*

¹⁵*NSF's National Optical-Infrared Astronomy Research Laboratory, 950 N Cherry Ave., Tucson, AZ 86719, USA*

ABSTRACT

The spatial inhomogeneity is one of the important features for understanding the reionization process; however, it has not yet been fully quantified. To map this inhomogeneous distribution, we simultaneously detect Ly α emitters (LAEs) and Lyman break galaxies (LBGs) at $z \sim 6.6$ from the Subaru/Hyper Suprime-Cam (HSC) large-area ($\sim 1.5 \text{ deg}^2 = 34000 \text{ cMpc}^2$) deep survey. We estimate the neutral fraction, x_{HI} , from the observed number density ratio of LAEs to LBGs, $n(\text{LAE})/n(\text{LBG})$ based on numerical radiative transfer simulation, in which model galaxies are selected to satisfy the observed selection function. While the average x_{HI} within the field of view is found to be $x_{\text{HI}} < 0.4$, which is consistent with previous studies, the variation of $n(\text{LAE})/n(\text{LBG})$ within the field of view for each 140 pMpc^2 is found to be as large as a factor of three. This may suggest a spatially inhomogeneous topology of reionization, but it also leaves open the possibility that the variation is based on the inherent large-scale structure of the galaxy distribution. Based on the simulations, it may be difficult to distinguish between the two from the current survey. We also find that LAEs in the high LAE density region are more populate high EW_0 , supporting that the observed $n(\text{LAE})/n(\text{LBG})$ is more or less driven by the neutral fraction, though the statistical significance is not high.

1. INTRODUCTION

The reionization process is the transition of the intergalactic medium (IGM) from a neutral to an ionized state. One of the important features of reionization is the spatial inhomogeneity, whose topology is closely related to the distributions of the ionizing sources, escape

fraction of ionizing photons, the clumpiness of the IGM, and the ionizing photon energy, and so on. Strong radiation from the first stars and galaxies ionized their surrounding neutral intergalactic medium, creating a sphere of ionized atomic hydrogen, an HII bubble (e.g., McQuinn 2016). The multiplication and progressively larger size of these HII bubbles resulted in the reionization of nearly all of the available neutral primordial gas, completing the process of cosmic reionization around $z \sim 6$. Therefore, we expect spatially inhomogeneous distribution of the neutral and ionized IGM, whose char-

characteristic physical scales and topology depend on the histories of clustering and luminosity of the reionizing sources. There is an active debate over whether faint galaxies (e.g., Finkelstein et al. 2019) or bright (e.g., Naidu et al. 2020) galaxies should play a more significant role in the reionization photon budget, but the reionization topology will vary greatly depending on which one contributes more. Previous studies have reported some observational evidence of spatially inhomogeneous reionization, primarily from the observations of large scatter of IGM transmission on the background quasars (e.g., Fan et al. 2006; Becker et al. 2015; Bosman et al. 2018; Yang et al. 2020). Recent observations continue to provide indirect evidence of large HII bubbles (e.g., Zheng et al. 2017; Castellano et al. 2018; Tilvi et al. 2020; Meyer et al. 2020; Hu et al. 2021).

The Ly α fraction $X_{\text{Ly}\alpha}$ is one of the widely used methods for assessing the neutrality of the IGM at the epoch of cosmic reionization (e.g., Stark et al. 2010; Ono et al. 2012; Curtis-Lake et al. 2012; Schenker et al. 2014; Tilvi et al. 2014; Cassata et al. 2015; see also a review by Ouchi et al. 2020). These studies derive $X_{\text{Ly}\alpha}$ as the fraction of Lyman break galaxies (LBGs) that show Ly α emission lines at $4 < z < 9$, suggesting the trend that the Ly α fraction abruptly drops from $z = 6$ to $z = 7$ in contrast to its monotonic increase from $z = 4$ to $z = 6$. This can be caused by resonant scattering by intervening neutral hydrogen in IGM during the reionization epoch. In addition to the decrease in the Ly α fraction, the decline in Ly α equivalent width (EW) at $z > 6$ has been observed in previous studies, suggesting the suppression of Ly α visibility (e.g., Treu et al. 2012, 2013; Hoag et al. 2019; Mason et al. 2019; Jung et al. 2020). However, identifying the Ly α emission lines generally requires spectroscopic observations of LBGs, which is too expensive to enlarge the sample size and survey area. Previous studies have limited the survey area to a maximum of about 0.1 deg^2 and the number of targets to about 70 (Stark et al. 2011; Schenker et al. 2014). Therefore, these studies are unable to depict the spatial variation of the neutral fraction x_{HI} , and only put the constraints on the averaged value over the survey volume.

To overcome this difficulty, we use a dataset of large-area ($\sim 1.5 \text{ deg}^2$) imagings from Subaru/Hyper Suprime-Cam (HSC; Furusawa et al. (2018); Kawanomoto et al. (2018); Komiyama et al. (2018); Miyazaki et al. (2018)). The large field of view (FoV) of HSC enables us to efficiently detect Lyman alpha emitters (LAEs) and LBGs and to illustrate the spatial inhomogeneity of reionization. In contrast to the previous studies, we detect LAEs based only on the photomet-

ric observations and construct LBG and LAE samples separately. Though the limiting luminosity of the LAE and LBG samples is not necessarily the same, we use a ratio of the number density of LAEs to that of LBGs $n(\text{LAE})/n(\text{LBG})$ as a proxy for the Ly α fraction. The same selection criteria as in the observation is applied to the model to consider the difference in limiting magnitude between the two populations when generating the model prediction of x_{HI} from $n(\text{LAE})/n(\text{LBG})$. One key importance here is that LBGs and LAEs must be simultaneously detected at almost the same redshift to measure $n(\text{LAE})/n(\text{LBG})$. For this purpose, we have installed a new intermediate-band filter, IB945, whose central wavelength is 9462 \AA with a full width at half maximum (FWHM) of 330 \AA . The IB945 can detect LBGs at $z \sim 6.6$, whose redshift range ($\Delta z = 0.4$) is narrower than that of the typical Lyman break selection ($\Delta z = 1.0$). With the wide FoV and the new filter, HSC is the only instrument in the world capable of carrying out this study.

In this paper, we use the imaging data taken by HSC Subaru Strategic Program (SSP; Aihara et al. 2018a)¹ and Cosmic HydrOgen Reionization Unveiled with Subaru (CHORUS) project (Inoue et al. 2020). This paper is constructed as follows. Section 2 describes the observational data we use. Sample selection is explained in Section 3. We show the distribution of the LAEs and LBGs and draw the $n(\text{LAE})/n(\text{LBG})$ map in Section 4. Section 5 describes the reionization simulation and discusses the neutral fraction and its spatial variation. We summarize this paper in Section 6.

Throughout this paper, we use the AB magnitude system (Oke & Gunn 1983). We adopt a Λ CDM cosmology with $h = 0.7$, $\Omega_{\text{M}} = 0.3$, and $\Omega_{\Lambda} = 0.7$, which is consistent with the recent *Planck* observations (Planck Collaboration et al. 2020).

2. OBSERVATIONAL DATA

We use the HSC-SSP S18A UltraDeep internal data release product of g , r , i , z , and Y broad-band (BB), and NB921 images taken from 2014 to 2018. The details of the SSP observations are described in Aihara et al. (2018a). We refer to Aihara et al. (2018b, 2019) for the data analysis and the catalog construction. The NB921 (Ouchi et al. 2018) has a central wavelength of 9215 \AA and a FWHM of 135 \AA . Figure 1 shows the transmission curves of the filters.

The IB945 images are taken through the CHORUS project (Inoue et al. 2020). We have carried out deep

¹ <https://hsc.mtk.nao.ac.jp/ssp/>

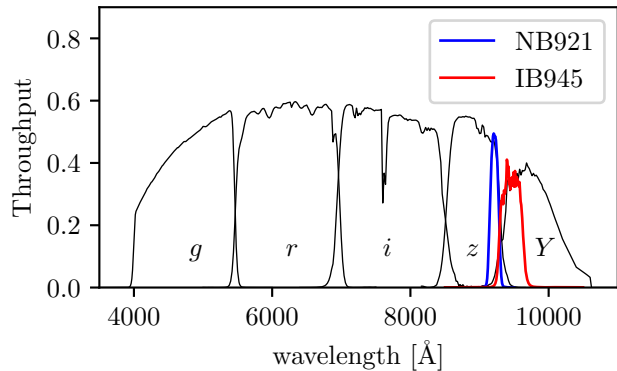


Figure 1. Filter transmission curves of the BB, NB, and IB filters. The blue and red lines show the NB921 and IB945 filters, respectively. The black solid lines represent the g -, r -, i -, z -, and y -band filters from left to right.

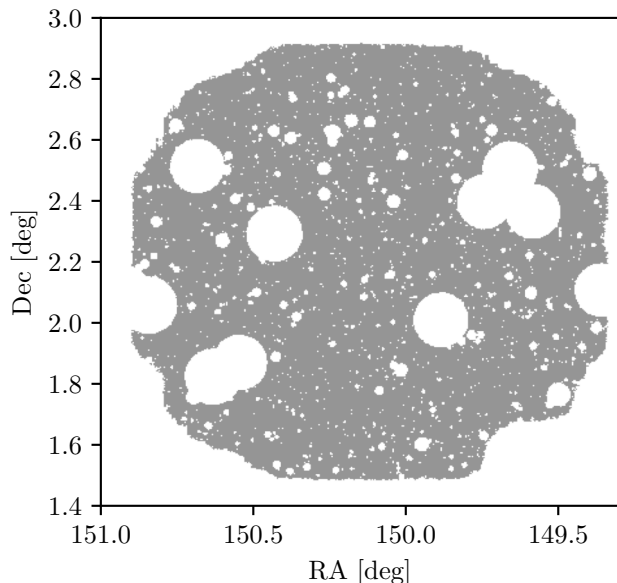


Figure 2. The effective survey area of our data. The mask regions that are combined in all band images are shown in white.

imaging observation with IB945 in the COSMOS field, which is one of the UltraDeep layers of the HSC-SSP. The HSC data are reduced with HSC pipeline version 6.7 (Bosch et al. 2018), which is based on Large Synoptic Survey Telescope (LSST) pipeline (Jurić et al. 2017; Ivezić et al. 2019; Bosch et al. 2019). The astrometry and photometric calibration is performed based on the data from Panoramic Survey Telescope and Rapid Response System 1 (Pan-STARRS1; Chambers et al. 2016; Schlafly et al. 2012; Tonry et al. 2012; Magnier et al. 2013). The final seeing size is $0''.66$. The survey area is divided into **tracts**, and each **tract** is divided into 9×9

Table 1. Image properties.

Filter	5σ limiting magnitude ^a	PSF [$''$] ^b
g	27.9	0.84
r	27.6	0.74
i	27.5	0.70
z	27.0	0.65
Y	26.4	0.77
NB921	26.3	0.68
IB945	25.9	0.66

^aThe 5σ limiting magnitude with a $1''.5$ aperture in the **patch** (4,4).

^bPSF size averaged in the entire FoV.

patches (Aihara et al. 2018a). Table 1 summarizes the details of the imaging data.

In our analysis, we use **forced** catalogs, in which photometry is measured at the fixed position in all band images. We use **convolvedflux** to measure the magnitude after smoothing as a source has the same PSF sizes in all the filters. The aperture diameter and the PSF size are $1''.5$ and $0''.84$, respectively.

We use **hscPipe** parameters and flags to exclude objects affected by saturated or bad pixels, and nearby bright stars. To ensure the images are sufficiently deep, we limit the survey field by using the **countinput** parameter. The **brightobject** mask is automatically generated in the pipeline (Coupon et al. 2018). Because the **brightobject** mask is not enough around the brightest stars, we visually check the images and add mask regions where the image is affected by the bright objects. The effective survey area of the IB945 image is 1.46 deg^2 as shown in Figure 2. Table 2 indicates the detail of the flags and parameters.

The limiting magnitude in each **patch** is calculated in the same way as Inoue et al. (2020). We distribute ~ 5000 apertures with $1''.5$ diameter per **patch** avoiding the masked regions and detected sources and derive the limiting magnitude by fitting the flux distribution with a Gaussian function. Sky subtraction is performed by a median in an annulus of $1''.0$ width and $2''.5$ inner diameter around the aperture. The spatial variations in the $1''.5$ aperture limiting magnitudes are shown in Figure 3.

3. SELECTION

3.1. LAE selection

We construct a $z \sim 6.6$ LAE catalog using the HSC data. The selection of LAEs is based on flux excess in NB compared to adjacent BB filters. We apply the color

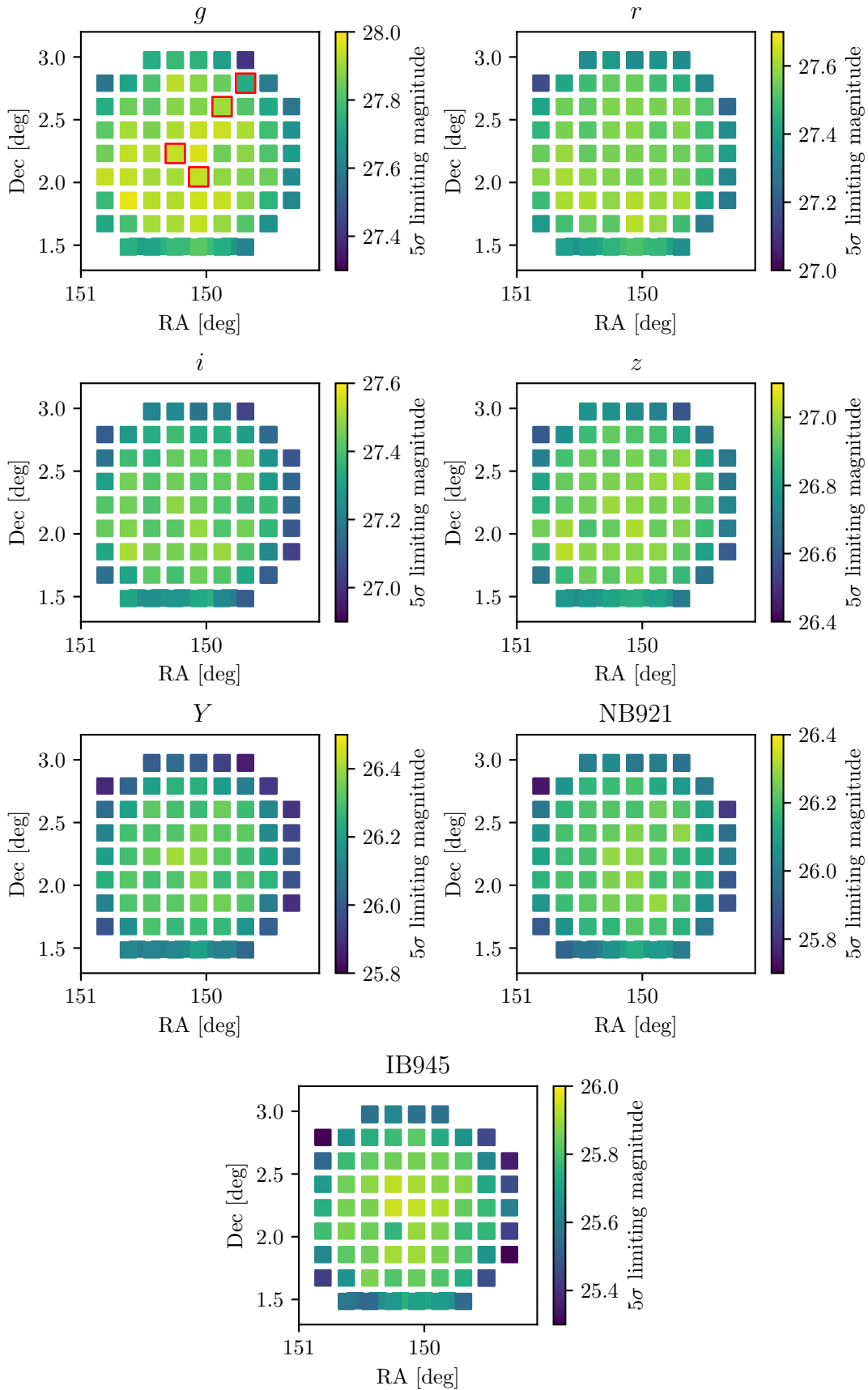


Figure 3. The 5σ limiting magnitudes in the $1''.5$ aperture and their spatial variation. The patches are overlapping due to the definition of the tracts and patches around DEC = 1.5° . The four red squares show the patches (4,4), (5,3), (6,6), and (7,7) from left to right.

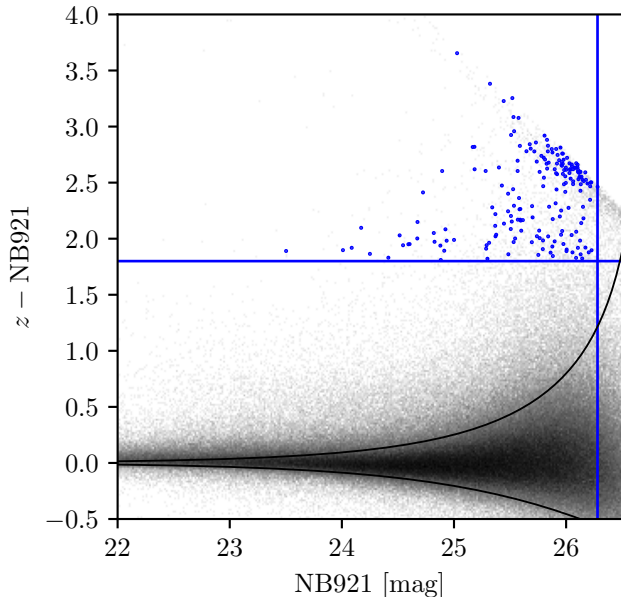


Figure 4. The color magnitude diagram of the LAE candidates. The blue points represent the LAE candidates. The horizontal blue line indicates the color criterion, $z - \text{NB921} = 1.8$. The vertical blue line shows the limiting magnitude in the patch (4,4). The black solid curve shows the 3σ error of the $z - \text{NB921}$ color given by equation (6). The grey dots represent all objects detected in NB921.

selection criteria similar to Shibuya et al. (2018a):

$$\text{NB921} < \text{NB921}_{5\sigma} \quad (1)$$

$$\& z - \text{NB921} > 1.8 \quad (2)$$

$$\& g > g_{5\sigma} \quad (3)$$

$$\& r > r_{5\sigma} \quad (4)$$

$$\& ((z < z_{3\sigma} \& i - z > 1.3) \text{ or } z > z_{3\sigma}), \quad (5)$$

where $\text{NB921}_{5\sigma}$, $g_{5\sigma}$, $r_{5\sigma}$, and $z_{3\sigma}$ represent 5σ or 3σ limiting magnitude in each filter. To remove low- z contaminants, we impose non-detection in a shorter wavelength than the Lyman limit and the existence of the Lyman break between i and z bands for sources detected in z band above 3σ level. The criteria for non-detection in g and r bands are relaxed to 5σ from 2σ cut of Shibuya et al. (2018a), because the 2σ cut significantly removes plausible LAE candidates. Since the g or r band image is very deep, if a very small 2σ level is used as the detection criterion, there are many cases where a small amount of noise is enough to cause the object to be judged as detected. In our dropout sample, detection of Lyman break is guaranteed by relaxing the criterion for non-detection. Relaxing the criteria may increase the low- z contaminants, but spectroscopic follow-up observations are necessary for quantitatively evaluate the contami-

nation. The $z - \text{NB}$ color threshold corresponds to the rest-frame Ly α equivalent width (EW_0) of $\text{EW}_0 > 14 \text{ \AA}$. The limiting magnitude in NB921 corresponds to the Ly α luminosity of $2 \times 10^{42} \text{ erg/s}$. We also consider 3σ error of the $z - \text{NB921}$ color as a function of the NB921 flux f_{NB} :

$$z - \text{NB921} > -2.5 \log \left(1 + 3 \frac{\sqrt{f_{z,1\sigma}^2 + f_{\text{NB},1\sigma}^2}}{f_{\text{NB}}} \right), \quad (6)$$

where $f_{z,1\sigma}$ and $f_{\text{NB},1\sigma}$ are 1σ flux error in z band and NB921, respectively. The 1114 objects are selected by the color-magnitude selection.

We visually inspect the images of LAE candidates to remove cosmic rays, false detection in NB, and sources that are apparently detected at shorter wavelengths but are considered as non-detection. In total, the number of LAE candidates is 189. Though the survey area is an order of magnitude larger than the previous studies (e.g., Stark et al. 2011; Schenker et al. 2014), the number of objects does not increase much as the survey depth is shallower by about one magnitude. Figure 4 shows the color-magnitude diagram of the LAE candidates.

The LAE candidates can be contaminated by low- z line emitters with a faint continuum, e.g., H α , [OIII], and [OII] emitters. NB-detected H α emitters, which are non-detected at short wavelengths, must have rest-frame $\text{EW}_0 > 160 \text{ \AA}$, which is exceptionally large (Fumagalli et al. 2012). To meet the color selection of $z - \text{NB} > 1.8$, the EW_0 of the [OII] and [OIII] emitters must be greater than 150 \AA and 270 \AA , respectively, but this EW is also extremely large (Reddy et al. 2018; Khostovan et al. 2016). Therefore, we can expect that the contamination of such low- z line emitters is negligible. Shibuya et al. (2018b) estimate contamination rates in the HSC LAE candidates from spectroscopic confirmations. The contamination rates are $\simeq 33\%$ and $\simeq 14\%$ for bright ($\text{NB} < 24 \text{ mag}$) and all LAE candidates, respectively. Given that we are using the same $z - \text{NB921}$ color cut as theirs, we expect the contamination rates in our sample are similar, though different criteria for non-detection of g and r bands may increase the contamination rate. Ono et al. (2021) construct an LAE sample from the same dataset. They use $z - \text{NB921} > 1.0$ color cut. They select LAE candidates with machine learning technique instead of the visual inspection. Our LAE catalog includes some fainter objects than theirs due to the difference in the measurement of the limiting magnitude. The number of our LAE candidates that meet their limiting magnitude is 60, and 31 out of the 60 LAE candidates are also included in their LAE catalog. Most

Table 2. The flags and parameters.

Name	Value	Filters	Description
<code>detect_is_tract_inner</code>	True	-	Source is in the inner region of a tract
<code>detect_is_patch_inner</code>	True	-	Source is in the inner region of a patch
<code>countinputs</code>	≥ 30	IB	Number of visits at a position of a source
<code>merge_peak</code>	True	NB for LAEs	peak detected in a given filter
<code>deblend_nChild</code>	0	$g, r, i, z, Y, \text{NB}, \text{and IB}$	Number of children a source has
<code>base_PixelFlags_flag_edge</code>	False	$g, r, i, z, Y, \text{NB}, \text{and IB}$	Source is inside exposure region
<code>base_PixelFlags_flag_saturatedCenter</code>	False	$g, r, i, z, Y, \text{NB}, \text{and IB}$	Source does not have any saturated pixels in the center
<code>base_PixelFlags_flag_bad</code>	False	$g, r, i, z, Y, \text{NB}, \text{and IB}$	Source does not have any bad pixels in the footprint
<code>base_PixelFlags_flag_bright_object</code>	False	$g, r, i, z, Y, \text{NB}, \text{and IB}$	Source footprint does not include pixels affected by bright objects
<code>base_PixelFlags_flag_bright_objectCenter</code>	False	$g, r, i, z, Y, \text{NB}, \text{and IB}$	Source center is not affected by bright objects
<code>ext_convolved_ConvolvedFlux_1.4_5_flag</code>	False	$z, Y, \text{and IB for LBGs}$ $i, z, \text{NB}, \text{and IB for LAEs}$	Flux measurement fails if true

of the LAE candidates that are not appeared in their catalog are fainter objects.

3.2. LBG selection

We construct a $z \sim 6.6$ LBG catalog based on Lyman break color selection technique, which is efficient for selecting sources with a sharp Lyman break and a blue UV continuum. Selection criteria are as follows:

$$Y < Y_{5\sigma} \quad (7)$$

$$\& g > g_{5\sigma} \quad (8)$$

$$\& r > r_{5\sigma} \quad (9)$$

$$\& z - Y > 1.2 \quad (10)$$

$$\& \text{IB945} - Y < 1.0 \quad (11)$$

$$\& z - \text{IB945} > 1.0. \quad (12)$$

To derive these criteria, we use spectral energy distribution (SED) models by CIGALE (Boquien et al. 2019). In this modeling, we use the Bruzual & Charlot (2003) single stellar population model and the Salpeter initial mass function (Salpeter 1955). Model parameters are a constant star formation history with an age of 50, 100, 200, and 400 Myr, metallicity of $Z/Z_{\odot} = 0.2$, the Calzetti extinction law with $E(B - V) = 0.0\text{--}0.4$ (Calzetti et al. 2000), and the IGM absorption of Meiksin (2006), which is the default IGM model of CIGALE. Figure 5 shows the evolutionary track of the model SED on the $\text{IB945} - Y$ vs. $z - Y$ plane. The limiting magnitude of the Y band almost corresponds to the rest-frame UV absolute magnitude (M_{UV}) of $M_{\text{UV}} < -20.5$ when assuming a flat continuum slope. By using IB945, the redshift distribution of LBGs can be made narrower than the typical z -dropout selection

(see Figure 9). We further explore the redshift distribution of our samples in Section 3.3.

The 589 objects are selected from the color selection. We carry out visual inspections to exclude false detection in the Y band, and sources that are apparently detected at shorter wavelengths but are considered as non-detection. Finally, the number of LBG candidates is 179. Unlike LAEs, cosmic rays are rarely contaminated, as it requires that they be detected in at least two Y and IB945 bands. The color-color diagram of the LBG candidates is shown in Figure 5. Seven LBG candidates are also included in the LAE catalog, which demonstrates that we detect LBGs at the similar redshift to the LAEs. The reason for the small number of sources selected for both LAE and LBG is that the limiting magnitudes of both samples are not the same. When calculating the neutral fraction from the sample, we take this difference into account and apply these selection criteria to the simulation model.

Since the $z - Y$ color of low- z galaxies is small, as shown in Figure 5, the contamination rate is expected to be low. However, as in the case of LAE selection, the 5σ limiting magnitude is used as a criterion for non-detection in the g - and r -bands, which may lead to increased contamination. The quantitative evaluation of the contamination rate is difficult unless we conduct systematic spectroscopic follow-up observations of the IB945-selected galaxies. Harikane et al. (2021) detect 27 $z \sim 7$ LBGs in the same field by using a $z - Y$ color criterion. Eighteen of their samples are also included in our LBG sample. Our LBG catalog contains more LBGs than their sample because of the differences in the color

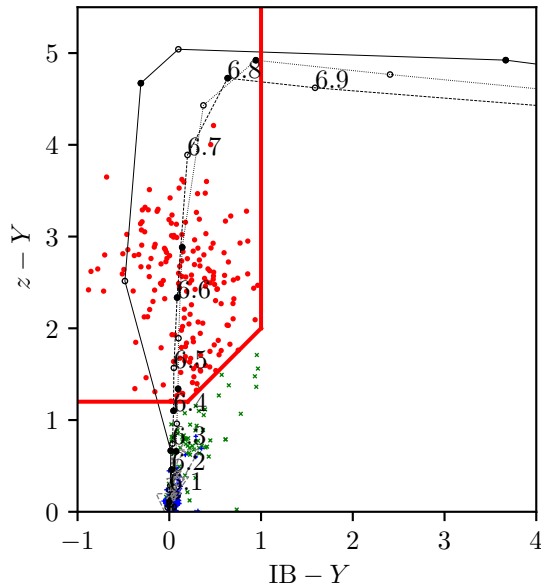


Figure 5. The color-color diagram of the LBG candidates. The red points represent the LBG candidates which pass the visual inspection. For sources fainter than 1σ level in the z band, z band magnitudes are replaced with 1σ limiting magnitude. The red solid line shows the LBG selection criteria. The black solid, dashed, and dotted lines show the track of LBG model SED constructed by CIGALE with $E(B - V) = 0.0, 0.2,$ and $0.4,$ respectively. The black circles indicate their redshift from $z = 5.5$ to $z = 7.0$ with $\Delta z = 0.1$ step. The green points indicate dwarf stars taken from Knapp et al. (2004), and the blue pluses show stars from Gunn & Stryker (1983). The dashed grey line shows the typical track of elliptical, Sbc, Scd, and irregular galaxies (Coleman et al. 1980) from $z = 0$ to 2.

selection criteria and the measurement of the limiting magnitude.

3.3. Completeness

We estimate the detection and selection completeness of our samples by the following Monte Carlo simulation. Here, the detection completeness is defined as the fraction of mock galaxies that are detected in the detection band, while the selection completeness is defined as the fraction of mock galaxies that satisfy the color selection criteria, which also takes detection completeness into account. To generate a mock LBG catalog, we use the same SED model as described in Section 3.2. In contrast to the mock LBG catalog, we generate the SED model of LAEs with a simple assumption of a δ -function shaped Ly α emission line, a flat ($f_\nu = \text{const.}$) UV continuum, and the IGM attenuation of Madau (1995). The mock LAEs have the EW of $10 < \text{EW}_0 [\text{\AA}] < 200$ following the EW distribution obtained from Shibuya et al. (2018a).

The redshift of the mock LAEs ranges from 6.50 to 6.66 with an interval of $\Delta z = 0.02$.

We randomly distribute the mock galaxies on the $g, r, i, z,$ and Y band, NB921, and IB945 images using BALROG (Suchyta et al. 2016). We consider the total magnitude of the mock galaxies in the range of $23 \leq m \leq 27$ with a 0.5 magnitude step in Y band and NB921 for LBGs and LAEs, respectively. We assume that the Sérsic profile with an index of 1.5 and a half-light radius of 0.4 pkpc, which are consistent with Shibuya et al. (2015, 2019) at $z \sim 6.6$. The BALROG makes use of GALSIM (Rowe et al. 2015) to simulate the profile of the objects and convolve it with the PSF size. The PSF model is constructed with PSFEX (Bertin 2011) from cutout images at each detection processed with SEXTRACTOR (Bertin & Arnouts 1996). We detect and measure the mock galaxies using hscPipe version 6.7 in the same way as described in Section 2.

The detection completeness is defined as a number fraction of the mock galaxies that are successfully detected in the detection band images (Y and NB921 for LBGs and LAEs, respectively). We regard sources that are detected within $0''.5$ from the positions of the mock galaxies and with a difference of 0.5 magnitude or less from the input magnitude as successfully detected objects (Inoue et al. 2020). We apply the same selection to the mock galaxies as described in Sections 3.1 and 3.2 and calculate the selection completeness of our LAE and LBG samples. The selection completeness is defined as a number ratio of the mock galaxies satisfying the selection criteria to all the mock galaxies. The LAE selection function considers $z - \text{NB}$ color. Since the wavelength ranges of filter transmission of z band and NB921 overlap, emission lines detected in NB do not necessarily satisfy the $z - \text{NB}$ color selection. It is important to consider the selection completeness for LAEs. The uncertainty of the completeness takes into account the Poisson errors of the numbers of the embedded and recovered mock galaxies.

As shown in Figure 3, the spatial variation of the limiting magnitude in the survey area is approximately circularly symmetric and the limiting magnitude becomes gradually shallow towards the edge of the FoV. We divide the survey area into four regions with respect to the distance from the center and assume that the completeness is constant in each region. We use the patches (4,4), (5,3), (6,6), and (7,7), which are 0, 16, 32, and 48 arcmin away from the center of the FoV (Figure 3). We carry out this simulation in the four patches to estimate the spatial variation of completeness in the FoV. Figure 6 shows the detection completeness for LBGs and LAEs. This figure shows slightly lower completeness at

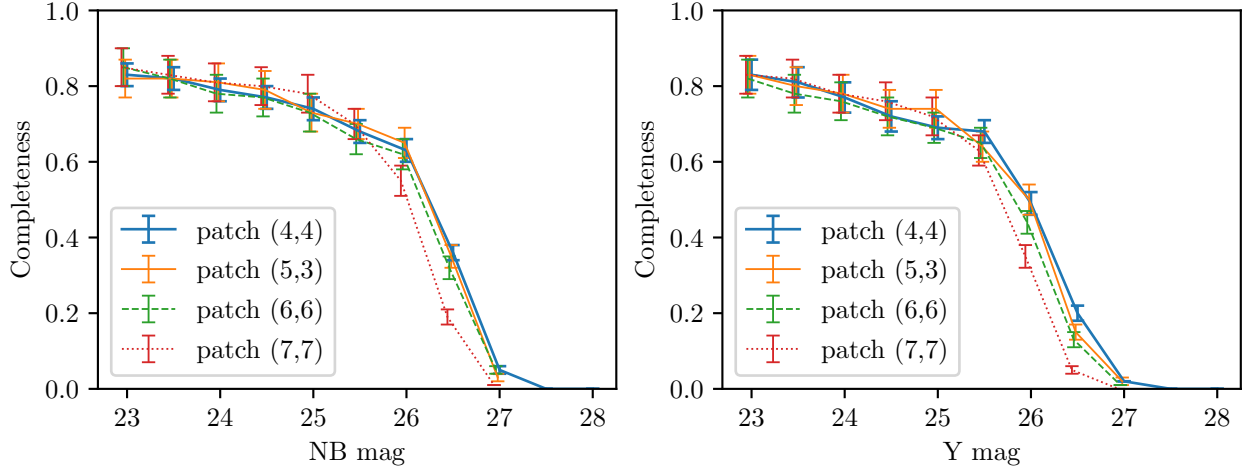


Figure 6. Detection completeness of the NB921 (left) and Y band (right) as a function of magnitude. Thick solid, thin solid, dashed, and dotted lines represent the results in patches (4,4), (5,3), (6,6), and (7,7), respectively. Data points are slightly shifted horizontally for clarity.

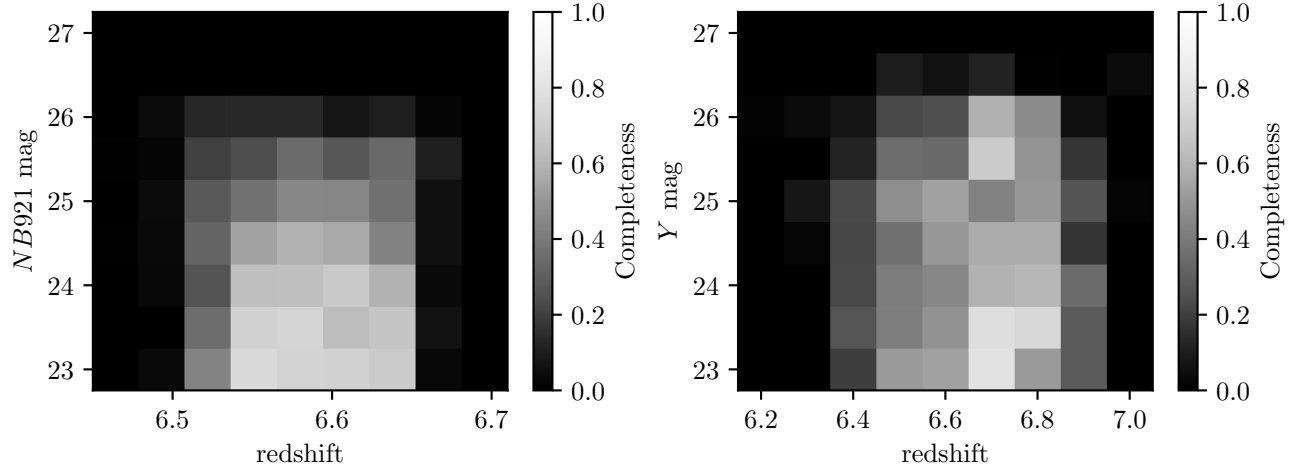


Figure 7. Selection completeness of our LAEs (left) and LBGs (right) as a function of magnitude and redshift in the patch (4,4).

the edge of the FoV. The detection completeness is less than unity even on the bright end. This is because the embedded mock galaxies overlap with the bright objects in the image. Figure 7 shows the selection completeness as a function of magnitude and redshift for LBGs and LAEs in the patch (4,4).

In Section 5.1.2, we sample model galaxies in the same redshift range as the observation to make comparisons. For this purpose, we derive the redshift distribution without taking detection incompleteness into account, which we call the selection function. We define the selection function as the selection completeness divided by the detection completeness. In each patch, we derive the selection function for each magnitude. The amplitude of the selection function of LAE strongly depends on the NB magnitude because the fainter objects have

larger uncertainty in the observed color, while the selection function of LBG has almost no changes in terms of the magnitude. We average the selection functions over the magnitude weighted with the observed number count. The error of the selection function is calculated from the uncertainty of the detection and selection completeness. Figure 8 shows the selection function of LAEs and LBGs. We do not find any systematic variations of the selection function in the four patches. The selection function should be less than or equal to unity, but there is one point that is greater than unity in the LBG selection function, which is just caused by the calculation. The selection completeness is calculated in each magnitude and redshift, while the detection completeness is averaged over redshift. Thus, the selection completeness is not necessarily smaller than the detection complete-

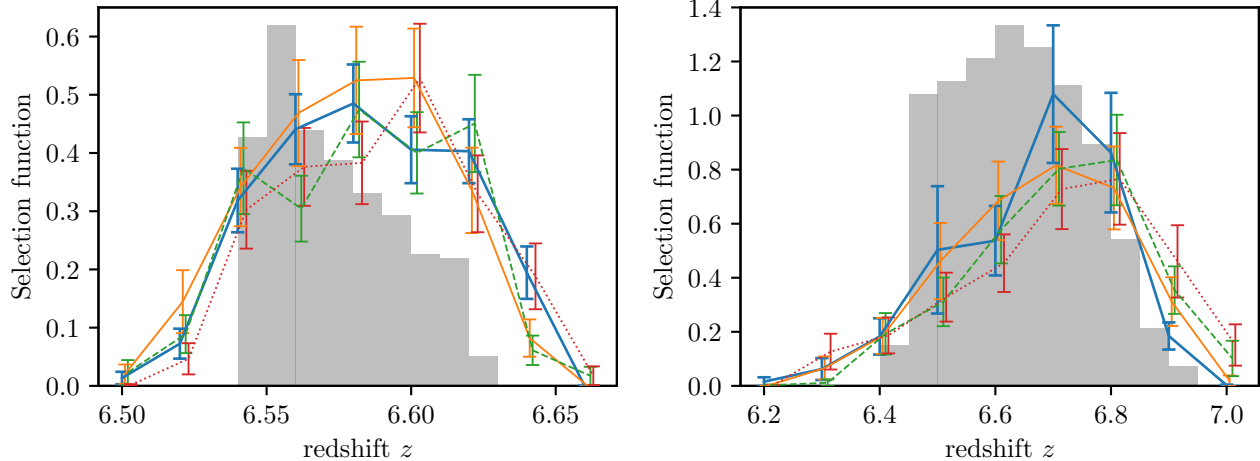


Figure 8. The selection function of the LAEs (left) and the LBGs (right). Colors indicate the patches in the same as Figure 6. Grey histograms show the redshift distribution of model LAEs and LBGs selected from the simulation box (Section 5.1.1). The amplitudes of the histograms are scaled for clarity.

ness. We also show in Figure 8 the redshift distribution of model galaxies (Section 5.1.1) selected with the same color selection criteria. The redshift ranges are similar to the selection functions while the peaks of the distribution are shifted to lower redshift. This is because higher redshift galaxies are more difficult to detect due to their fainter magnitude. In Figure 9, we compare the selection function of the samples. While the width of the LBG selection function is broader than that of LAEs, it is narrower than that of the typical z -dropout selection. This confirms that IB945 allows us to detect LBGs at similar redshift to LAEs. The remaining difference in the selection function between LBG and LAE is taken into account in the model galaxies to be compared, along with the difference in the limiting magnitude, so as to have exactly the same selection function with the observation (Section 5.1.2).

4. RESULTS

4.1. Surface density

Applying the selection criteria described in Section 3, we obtained 179 LBGs and 189 LAEs at $z \sim 6.6$. Figures 10 and 11 show the surface densities of LBGs and LAEs as a function of magnitude, respectively. Since the redshift range (Δz) of our LBG selection is different from that of Bouwens et al. (2015), we correct it by the width of the selection function estimated in Section 3.3. The surface densities of LBGs and LAEs corrected by the detection completeness are found to be consistent with the previous studies. The surface density of LAEs is lower than that of Ouchi et al. (2010), though this is because the `MAG_AUTO` of `SEXTRACTOR`, which they use as the total magnitude, is biased towards brighter magnitudes. By integrating the surface density corrected by

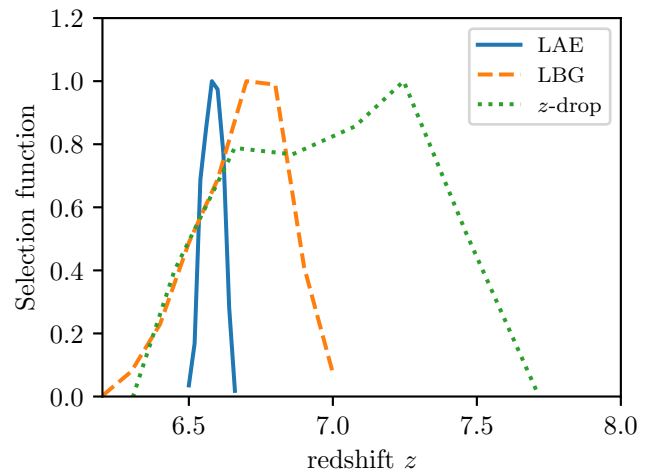


Figure 9. Normalized selection functions of the samples. The blue solid and the orange dashed line represent the LAEs and LBGs, respectively. We also show the selection function of z -dropout galaxies from Ono et al. (2018) with the green dotted line for comparison.

the detection completeness down to the limiting magnitudes, we obtain $n(\text{LAE})/n(\text{LBG}) = 0.76 \pm 0.10$ as an average of the entire FoV.² In this calculation, we only consider the Poisson error and the error of the completeness as the uncertainty of $n(\text{LAE})/n(\text{LBG})$.

To evaluate the scatter of $n(\text{LAE})/n(\text{LBG})$, we distribute ~ 5000 apertures of 10–30 arcmin radii on the survey area and count the number of LAEs and LBGs

² Note that this value has a different definition from the so-called Ly α fraction, which has been measured so far. Throughout this paper, we use the term $n(\text{LAE})/n(\text{LBG})$ to distinguish it from the Ly α fraction. See section 5.1.3 for a comparison of the two.

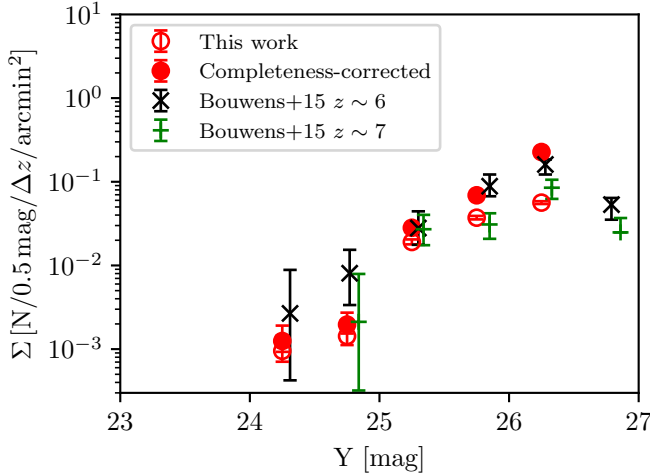


Figure 10. Surface number density of LBGs at $z \sim 6.6$ as a function of Y band magnitude. Filled and open circles represent the raw and the detection completeness corrected surface densities of our $z \sim 6.6$ LBGs ($\Delta z = 0.4$), respectively. Black crosses and green pluses indicate the surface densities of $z \sim 6$ ($\Delta z = 0.8$) and 7 ($\Delta z = 1.0$) galaxies of Bouwens et al. (2015), respectively.

within them. We exclude apertures where the masked regions cover more than 20% of the apertures. Figure 12 shows the median and scatter of $n(\text{LAE})/n(\text{LBG})$ as a function of aperture radii. There is deviation from the value calculated for the entire FoV ($n(\text{LAE})/n(\text{LBG}) = 0.76 \pm 0.10$) even with $30'$ apertures. This is because the number ratio in the entire FoV is derived by integrating the number density down to the limiting magnitude, which is a little different from counting the numbers in the apertures. Both approaches would give consistent results, but the difference in procedure of counting and completeness correction may cause slightly different results.

To see the spatial variation of $n(\text{LAE})/n(\text{LBG})$ over the field, we use $20'$ (~ 50 cMpc) radius aperture in the following analysis. In general, using a small aperture ($r_{\text{ap}} < 15'$) will result in a larger variation of $n(\text{LAE})/n(\text{LBG})$, as expected, because fewer objects are contained in the aperture. On the other hand, an aperture of $> 25'$ radius, which is too large compared to the FoV of HSC, is not appropriate for the study of spatial inhomogeneity. With the $20'$ radius, the field averaged $n(\text{LAE})/n(\text{LBG})$ is $0.84^{+0.23}_{-0.27}$. Since this calculation takes the spatial variation of $n(\text{LAE})/n(\text{LBG})$ between the apertures into account, the uncertainty is larger than that described above. The difference between the maximum and minimum values is as large as a factor of three. In the following, we use this value as our result of $n(\text{LAE})/n(\text{LBG})$.

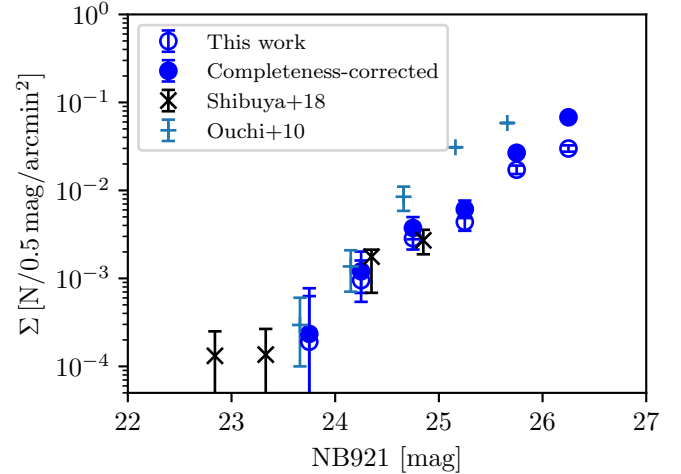


Figure 11. Surface density of LAEs at $z = 6.6$ as a function of NB921 magnitude. Filled and open circles represent the raw and the detection completeness corrected surface densities of our $z \sim 6.6$ LAEs, respectively. For comparison, we also plot results of Shibuya et al. (2018a) and Ouchi et al. (2010). The points are slightly shifted horizontally for clarity.

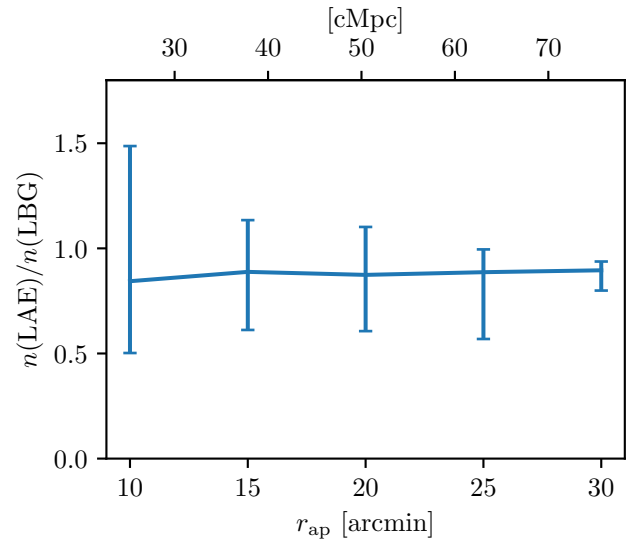


Figure 12. The median and 68 percentile range of $n(\text{LAE})/n(\text{LBG})$ in the FoV as a function of aperture size.

4.2. Spatial distribution

We calculate the density distribution using the Gaussian kernel density estimation. The surface density at a coordinate $X = (\text{RA}, \text{Dec})$ is given as

$$\sigma(X) = \sum_i K(X, X_i), \quad (13)$$

where K is the kernel function and $X_i = (\text{RA}_i, \text{Dec}_i)$ is the coordinate of the i -th galaxy. We choose a Gaussian

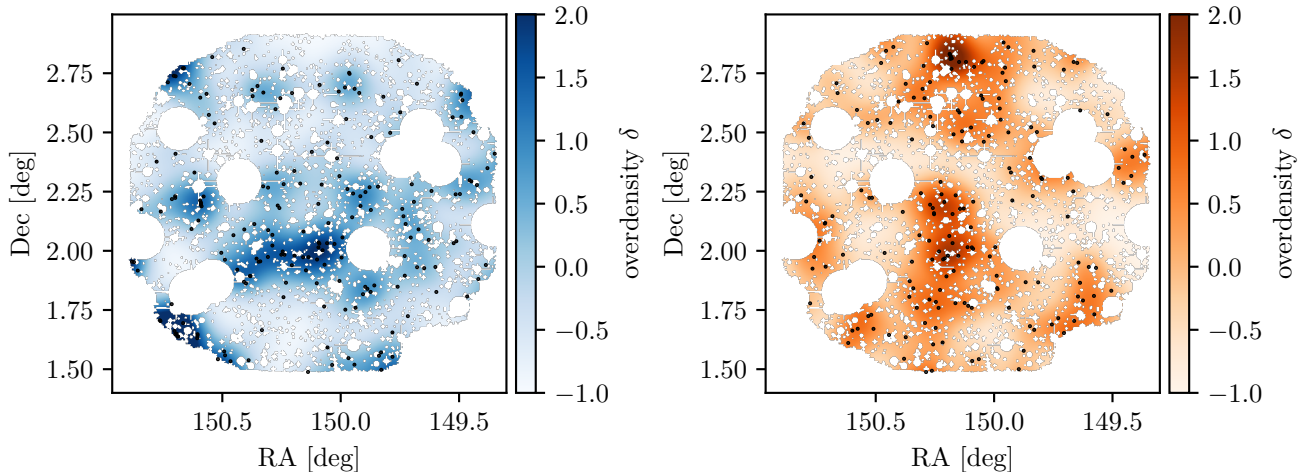


Figure 13. Boundary corrected density distribution of the LAEs (left) and LBGs (right). Black dots indicate the distribution of candidates of the LAEs and LBGs. Color bar represents the overdensity $\delta = (\sigma - \bar{\sigma})/\bar{\sigma}$. Masked regions are shown in white (see Figure 2).

as the kernel function:

$$K(X, X_i) = \frac{1}{2\pi\lambda^2} \exp\left(-\frac{r_i^2}{2\lambda^2}\right), \quad (14)$$

where r_i is the projected separation between X and X_i , and λ is the bandwidth parameter. The optimal bandwidth is calculated by maximizing the likelihood cross-validation (LCV; HALL 1982) in the same way as Chartab et al. (2020). The LCV is defined as

$$\text{LCV}(\lambda) = \frac{1}{N} \sum_{k=1}^N \log \sigma_{-k}(X_k), \quad (15)$$

where N is the total number of the objects and $\sigma_{-k}(X_k)$ is the surface density at the position (X_k) calculated excluding the k -th object. The optimized values are 3'.63 and 3'.75 for LBGs and LAEs, respectively. We adopt 4'.00 as the common bandwidth for LBGs and LAEs to compare them under the same condition. The spatial inhomogeneity of the depth is corrected with the detection completeness by assuming the circularly symmetric variation as described in Section 3.3.

Since the survey area is limited and has the masked regions, correcting the boundary effect is necessary. The true density distribution is estimated as (see Chartab et al. 2020; Jones 1993):

$$\sigma_{\text{true}}(X) = \frac{\sigma(X)}{\int_S K(X, X_i) dS}, \quad (16)$$

where the integration is calculated over the effective area of the survey field (S).

We define the overdensity δ as

$$\delta = \frac{\sigma - \bar{\sigma}}{\bar{\sigma}}, \quad (17)$$

where $\bar{\sigma}$ is the mean density averaged over the entire effective survey area after the completeness correction and the boundary correction. Figures 13 shows the density distribution of LBGs and LAEs, respectively. The LAE overdensity regions located slightly south of the center of the FoV are consistent with the results reported in Higuchi et al. (2019) and Zhang et al. (2020).

Using the whole sample of LBGs and LAEs, we draw the map of $n(\text{LAE})/n(\text{LBG})$. From Figure 14, it is interpreted that the reionization is proceeding in the high LAE density region, while it is delayed in the low LAE density region, though the intrinsic distribution of these galaxy populations must also be taken into account, which is discussed in Section 5.1.5.

5. DISCUSSION

5.1. Neutral fraction

5.1.1. Reionization simulation

We carry out a reionization simulation to predict the neutral fraction x_{HI} from $n(\text{LAE})/n(\text{LBG})$ based on Inoue et al. (2018). Simulating star formation and ionizing photon escape requires high-resolution radiative hydrodynamical (RHD) simulations. However, an RHD simulation in a large-scale (> 100 cMpc) box is not feasible because of the huge numerical costs. Therefore, we divide the simulation into following two steps. First, we conduct a high-resolution RHD simulation to model galaxies and IGM in a 20 cMpc^3 box. The RHD simulation takes into account radiative feedback, which regulates star formation. Then, the recipe constructed in the first step is used for solving the radiative transfer of ionizing photons in a large-scale N -body simulation in a box of $(162 \text{ cMpc})^3$. Inoue et al. (2018) present several models in terms of the production rate and the

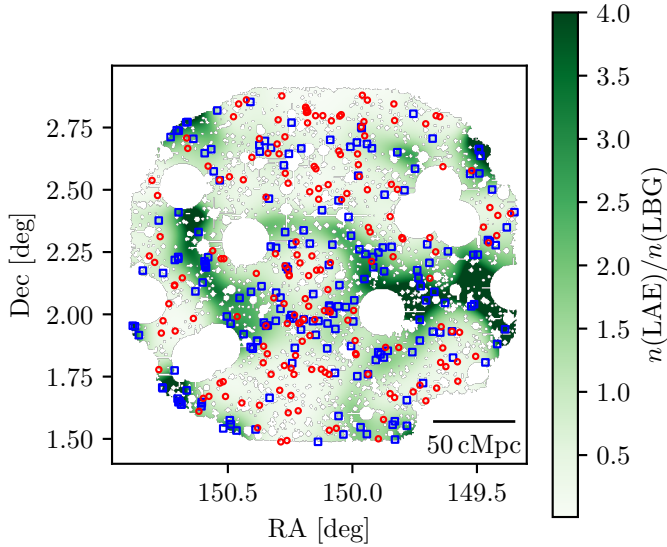


Figure 14. The map of $n(\text{LAE})/n(\text{LBG})$. The color map is constructed by dividing the density distribution of LAEs by that of LBGs (Figure 13). The blue squares and red circles show the distribution of LAEs and LBGs, respectively.

escape fraction of Ly α photons to simulate LAE SED. They find that the Model G reproduces the observed luminosity function, auto correlation function, and LAE fraction; therefore, we adopt Model G. In the Model G, the Ly α photon production rate is determined as a function of halo mass without any fluctuations. The Ly α escape fraction in the Model G depends on halo mass with a fluctuation to model the stochasticity in the transfer of Ly α photons. The reionization simulation assumes two models, the Late and Mid reionization models. The mean neutral fractions of the Late and Mid reionization models at $z \sim 6.6$ are 0.4 and 0.0, respectively. The detail of this simulation is described in Inoue et al. (2018). We generate 20 (10 for the Late reionization and the other 10 for Mid reionization) light cone outputs from $z = 5.5$ to $z = 9$ by randomly shifting and rotating the snapshots of the simulation box. Each light cone output has a $\sim 1 \text{ deg}^2$ FoV.

5.1.2. Correlation between Ly α fraction and neutral fraction

Using the simulation described above, we derive the relation between x_{HI} and $n(\text{LAE})/n(\text{LBG})$. We select model LAEs and LBGs in the light cones based on exactly the same selection functions (Figure 8) as observed in Section 3.3 to take into account the difference in the redshift range between the observed LAEs and LBGs. The model galaxies are randomly chosen according to the value of the selection function at their redshift. The model LAEs meet the Ly α luminosity of $L_{\text{Ly}\alpha} > 2.5 \times 10^{42} \text{ erg s}^{-1}$ and $\text{EW}_0 > 14 \text{ \AA}$, and the

model LBGs have the rest-frame UV absolute magnitude of $M_{\text{UV}} < -20.3$. These conditions are similar to those estimated from the selection criteria described in Sections 3.1 and 3.2. While we use the two reionization models, the neutral fractions are concentrated around $x_{\text{HI}} = 0.4$ and 0.0 at $z = 6.6$. To obtain the continuous relation over a wide range of x_{HI} , we shift the selection function along the redshift axis with $\Delta z = 0.1$ steps in a range of $6 < z < 8$ without changing the shape, and we sample the model LAEs and LBGs at each redshift. We assume a little evolution of both galaxy populations over $6 < z < 8$. We count $n(\text{LAE})$ and $n(\text{LBG})$ in randomly distributed apertures with radii of 20 arcmin ($\sim 50 \text{ cMpc}$), then calculate $n(\text{LAE})/n(\text{LBG})$. The neutral fraction is calculated in each aperture; averaged over the volume of the aperture with $20'$ radius and $\Delta z = 0.1$ ($\sim 40 \text{ cMpc}$) at the peak of the selection functions. Because the variation from different light cones is small, we combine all the 20 light cone outputs. In general, the Mid reionization model shows higher redshift than the Late reionization model at the same x_{HI} . Despite the difference in redshift, the both reionization models show similar results of $x_{\text{HI}}-n(\text{LAE})/n(\text{LBG})$ relation; therefore the effect of redshift evolution on the relation is considered to be negligible over $6 < z < 8$.

We show in Figure 15 the relation between $n(\text{LAE})/n(\text{LBG})$ and x_{HI} . The $n(\text{LAE})/n(\text{LBG})$ is inversely correlated with x_{HI} though the relation flattens out in the range of $x_{\text{HI}} < 0.25$ because most LAEs reside in ionized bubbles and their Ly α lines are less sensitive to the neutral gas in the highly ionized universe.

5.1.3. Field averaged neutral fraction and comparisons with previous studies

In Section 4.1, we obtain $n(\text{LAE})/n(\text{LBG}) = 0.84^{+0.23}_{-0.27}$ as an average of the entire FoV. By using the relation shown in Figure 15, we estimate the neutral fraction averaged over the survey field as $x_{\text{HI}} < 0.4$ by the 1σ range of $n(\text{LAE})/n(\text{LBG})$. In addition to the large scatter in $n(\text{LAE})/n(\text{LBG})$ in the simulation data, observed scatter in $n(\text{LAE})/n(\text{LBG})$ is large due to the shallow depth of the observation. The constraint for x_{HI} is only given as an upper limit. Deeper observations are required to more strictly constrain x_{HI} .

Since the faintest objects, the completeness of which is low (~ 0.5), have a dominant contribution to the total number of objects, this could be prone to uncertainty. To address this problem, we use the objects that are 0.5 mag brighter than the limiting magnitude and derive x_{HI} in the same way as described above. When calculating the $n(\text{LAE})/n(\text{LBG})-x_{\text{HI}}$ relation from the simulation model, we also use 0.5 mag brighter selection criteria for the model LBGs. We raise the lower limit of

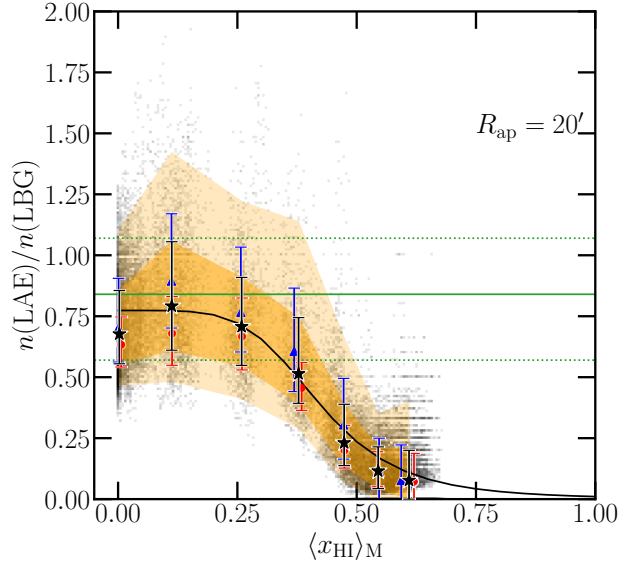


Figure 15. The relation between $n(\text{LAE})/n(\text{LBG})$ and the neutral fraction x_{HI} . The background grey colors show the all data points calculated in the light cone outputs, and the red circles and blue triangles show their median and 16th–84th percentile range for the Late and Mid reionization models, respectively. The black stars take into account both reionization models. The black curve and the orange shade indicate the median and the 68 and 95 percentile ranges of this relation. The horizontal solid and dashed green lines show the median and the 1σ scatter of the observed $n(\text{LAE})/n(\text{LBG})$, respectively.

the $\text{Ly}\alpha$ luminosity of the model LAE selection by $\times 1.6$ (corresponding to 0.5 mag brighter) since in the model, LAE selection is not based on photometric magnitude. The numbers of the model LBGs and LAEs decrease by factors of 0.3 and 0.4 with the 0.5 mag brighter selection criteria, respectively. This is consistent with the surface density of the observed LBGs and LAEs (Figures 10 and 11). The same result is obtained in this analysis; therefore, the x_{HI} estimate is found to be robust. In Appendix A, we describe the other selection procedures to further explore the robustness of our results.

In previous studies, the $\text{Ly}\alpha$ fraction $X_{\text{Ly}\alpha}$ is defined as the fraction of LBGs that show a $\text{Ly}\alpha$ emission line. These studies spectroscopically confirm $\text{Ly}\alpha$ emission lines among their photometric LBG sample. On the other hand, the redshift range and the limiting magnitude of our LAEs and LBGs are not exactly the same since we detect them separately. To compare our result with the $\text{Ly}\alpha$ fraction estimates of the previous studies $X_{\text{Ly}\alpha}^{25}$, we additionally constrain LAE as detected in Y band with 5σ significance ($Y < Y_{5\sigma}$). The Y band magnitude is a proxy for the rest-frame UV continuum flux, and $Y_{5\sigma}$ corresponds to $M_{\text{UV}} < -20.3$, which is similar to the depth of the LBG sample. We also limit

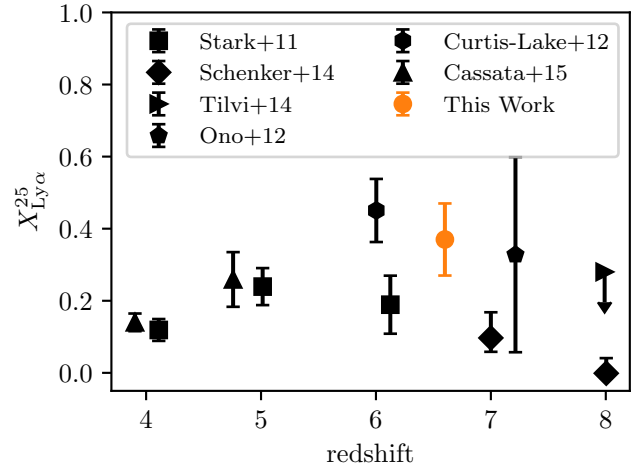


Figure 16. $\text{Ly}\alpha$ fraction $X_{\text{Ly}\alpha}^{25}$ as a function of redshift. The previous results are taken from Stark et al. (2010); Schenker et al. (2014); Tilvi et al. (2014); Ono et al. (2012); Curtis-Lake et al. (2012); Cassata et al. (2015).

LAEs with $\text{EW}_0 > 25 \text{ \AA}$. The EW_0 is calculated from the photometry in NB921 and the Y band. The number of LAEs that satisfy $Y < Y_{5\sigma}$ and $\text{EW}_0 > 25 \text{ \AA}$ is 15. Since the redshift range is different between LBGs and LAEs, we correct the difference by multiplying the ratio of the widths of the selection functions described in Section 3.3. Figure 16 shows the comparison of $X_{\text{Ly}\alpha}^{25}$ with the previous studies. Overall, our measurement of the field-averaged $n(\text{LAE})/n(\text{LBG})$ is consistent with the $X_{\text{Ly}\alpha}^{25}$ estimates of the previous studies within the error.

5.1.4. Spatial inhomogeneity of neutral fraction in the simulation box

As shown in Figure 14, we find the spatial variation of $n(\text{LAE})/n(\text{LBG})$. The $n(\text{LAE})/n(\text{LBG})$ map could be converted to x_{HI} map using Figure 15 to see a possible spatial inhomogeneity in the reionization process. However, since the two are almost uncorrelated for $x_{\text{HI}} < 0.25$, and the relation has a large scatter, it may be difficult to draw x_{HI} map from the observed data. Thus, we will use only the simulated data to see the spatial correlation between $n(\text{LAE})/n(\text{LBG})$ and x_{HI} . We average x_{HI} in a redshift slice of $6.54 < z < 6.63$. The selections of LAEs and LBGs are based on the color and magnitude in the same as the observation (Section 3), and we calculate $n(\text{LAE})/n(\text{LBG})$ in the same way as described in Section 4.2. Figure 17 shows the x_{HI} and $n(\text{LAE})/n(\text{LBG})$ map at $z = 6.6$ in one of the light cone models. We find a moderate correlation (correlation coefficient $r = -0.25$ and the p-value $p < 0.001$) between x_{HI} and $n(\text{LAE})/n(\text{LBG})$ when we divide the map into a grid with $1'$ (2.5 cMpc) side as shown in Figure 18. The

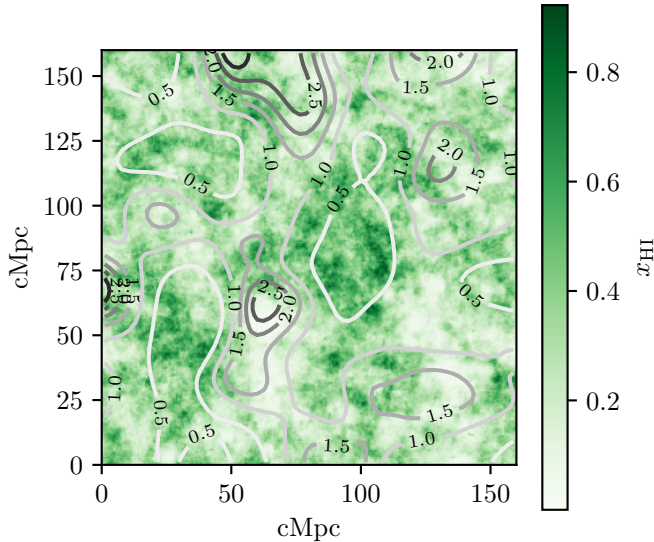


Figure 17. x_{HI} map and $n(\text{LAE})/n(\text{LBG})$ distribution in a simulation box of the Late reionization model. The green color shows the x_{HI} and the contours indicate the $n(\text{LAE})/n(\text{LBG})$.

apertures near the edge of the simulation box have less effective area overlapping with the simulation box, increasing the uncertainty of the relation. When we limit to the central region with a square of 80 cMpc per side, where boundary effect is small, the correlation becomes strong ($r = -0.47$ and $p < 0.001$). The result, at least in the simulation, demonstrates that the spatial variation of $n(\text{LAE})/n(\text{LBG})$ seen in Figure 14 implies the patchy reionization topology, i.e., the reionization is proceeding in the high LAE density region, while it is delayed in the low LAE density region. The high LAE density regions could correspond to the HII bubbles at $z \sim 6.6$.

5.1.5. Is the observed inhomogeneity caused by patchy reionization or intrinsic LSS?

In the previous section, we discuss a possible reionization topology from our observed spatial variation of $n(\text{LAE})/n(\text{LBG})$, although the number ratio of LAEs and LBGs, $n(\text{LAE})/n(\text{LBG})$ could depend also on their intrinsic distribution, the large scale structure (LSS). To distinguish the reionization topology from the LSS, we estimate the intrinsic scatter of $n(\text{LAE})/n(\text{LBG})$ without the IGM attenuation from the simulation data. The simulation calculates three kinds of Ly α luminosities; intrinsic, escaped from a halo, and transmitted through IGM. The third one is the Ly α luminosity with the IGM absorption and the second one is that without the IGM absorption ($x_{\text{HI}} = 0$). We compare the scatter of $n(\text{LAE})/n(\text{LBG})$ using the two Ly α luminosities in selecting LAEs. The reionization inhomogeneity further increases the scatter of $n(\text{LAE})/n(\text{LBG})$ in addition to

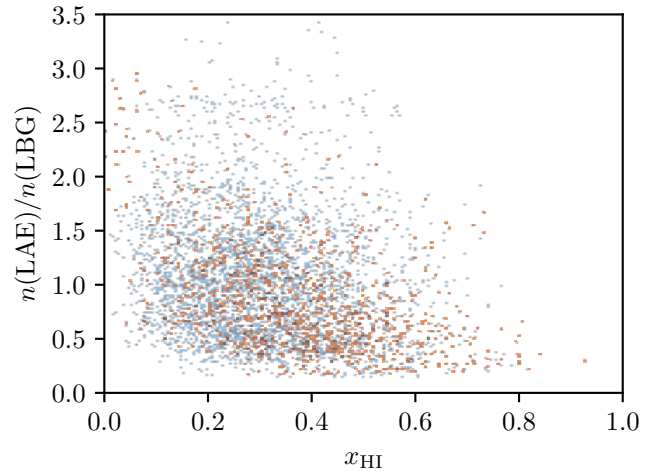


Figure 18. The relation between x_{HI} and the $n(\text{LAE})/n(\text{LBG})$ in the simulation box when dividing the map in Figure 17 into a grid with $1'$ (2.5 cMpc) side. The blue points show whole region shown in the map, and the orange points are from the central region with a square of 80 cMpc per side (25% of the total area of the simulation box).

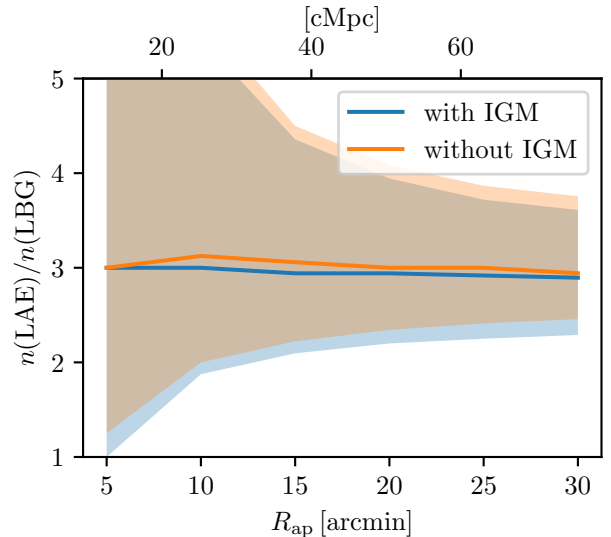


Figure 19. The median and 1σ scatter of $n(\text{LAE})/n(\text{LBG})$ as a function of aperture size in the Late reionization model. The blue and orange indicate with and without IGM absorption. The absolute value of $n(\text{LAE})/n(\text{LBG})$ is different from Figures 12 and 15 because LAE and LBG are both selected with the top-hat redshift distribution of $\Delta z = 0.1$.

the intrinsic scatter due to the LSS. Therefore, if we can confirm that the scatter with IGM is larger than that without IGM, we can conclusively distinguish between the two. Because in the Mid reionization model ($x_{\text{HI}} = 0.0$ at $z = 6.6$) the difference between the two

Ly α luminosities is negligible, we use the Late reionization model ($x_{\text{HI}} = 0.4$ at $z = 6.6$) in this analysis.

We select LAEs and LBGs in the same as Section 5.1.2, but we adopt the top-hat redshift distribution of $\Delta z = 0.1$ for LAEs and LBGs at $z = 6.6$ (see Appendix A). The number of LBGs does not change with or without IGM absorption, while the number of LAEs with the IGM absorption is smaller by a factor of 0.6 than that without the IGM absorption. In this comparison, the number of objects in both cases with and without IGM absorption, should be comparable, because we need to compare the scatter of both cases, as distinct from the difference in Poisson errors. Therefore, we randomly choose LAEs with the probability of 0.6 in the case of no IGM attenuation. In the case of IGM absorption, the Ly α attenuation depends on the neutral fraction, random choosing enables uniform reduction of the number of LAE without being affected by IGM absorption. Choosing randomly increases the uncertainty, but its effect is negligibly small. We distribute ~ 5000 apertures on the FoV and calculate $n(\text{LAE})/n(\text{LBG})$ within them. When the area overlapping with the simulation box is less than 80% of the aperture, we exclude the aperture, which degrades the result due to the large Poisson error. Varying the aperture radius from 5' to 30' (corresponding to 1.6–10 pMpc), we show in Figure 19 the scatter of $n(\text{LAE})/n(\text{LBG})$ with and without the IGM absorption. There is no difference between them probably due to the small number of the sample or a low neutral fraction at $z \sim 6.6$; therefore we conclude that distinguishing the reionization topology from the LSS may be difficult with this survey depth.

To investigate how deep observation is required for this aim, we carry out the same analysis including fainter objects in the simulation. We change the limiting Ly α luminosity down to $L_{\text{Ly}\alpha} > 2.5 \times 10^{41}$ erg/s with 0.2 dex interval and the limiting rest-frame UV absolute magnitude down to $M_{\text{UV}} < -17.5$ mag with 0.5 mag step. To match the expected number of LAEs with and without the IGM absorption, we randomly choose LAEs without the IGM absorption as described above. Figure 20 shows the scatter of $n(\text{LAE})/n(\text{LBG})$ within the apertures with 20' radius between with and without the IGM absorption as a function of limiting Ly α luminosity. The error bars are calculated by bootstrapping the model galaxies before calculating $n(\text{LAE})/n(\text{LBG})$ within the apertures. When we include the fainter objects the scatter of $n(\text{LAE})/n(\text{LBG})$ becomes smaller. However, we cannot find significant difference between with and without IGM absorption in the simulation even with two magnitude deeper observations (limiting luminosity $L_{\text{Ly}\alpha} \sim 4 \times 10^{41}$ erg/s) than the current survey.

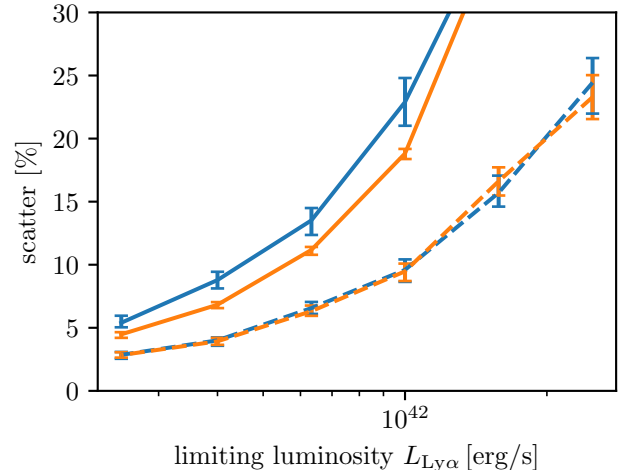


Figure 20. The scatter of $n(\text{LAE})/n(\text{LBG})$ relative to the median value as a function of limiting Ly α luminosity in the Late reionization model. Colors are the same as Figure 19. The dashed (solid) lines show the result of $z = 6.6$ (8.0). The grey dotted line shows the current survey depth. The error bars are estimated by bootstrapping the model galaxies before calculating $n(\text{LAE})/n(\text{LBG})$ within apertures.

At $z = 6.6$, IGM absorption hardly decreases the number of faint objects since the neutral fraction is not so high ($x_{\text{HI}} \sim 0.4$). That seems to be one of the reasons why we cannot see significant difference between with and without IGM absorption. We carry out the same analysis at $z = 8.0$ ($x_{\text{HI}} \sim 0.8$) to verify that the comparison of $n(\text{LAE})/n(\text{LBG})$ can distinguish reionization topology from the LSS. Since the number of objects declines at higher redshift, we use $\Delta z = 0.4$ at $z = 8.0$. In the same way as $z = 6.6$, we derive the scatter of $n(\text{LAE})/n(\text{LBG})$ as a function of limiting Ly α luminosity. We might be able to detect a difference between with and without IGM absorption seen in Figure 20 assuming deep observations (limiting luminosity $L_{\text{Ly}\alpha} \sim 4 \times 10^{41}$ erg/s) while the difference is small. This suggests that observation at the earlier phase of reionization may be able to detect spatially inhomogeneous nature in the universe with a sufficient amount of neutral hydrogen.

The variance of $n(\text{LAE})/n(\text{LBG})$ in the simulations used in this study is so large that there is no clear difference in the scattering with and without IGM absorption, as shown in Figures 19 and 20. This large variance may be due to uncertainties in the model, such as stochastic processes in the LAE model, as well as Poisson noise and the LSS. When deeper observational data are considered, Poisson noise decreases, but the variance from the LSS and LAE models still exceeds the variance from x_{HI} at $z = 6.6$ (Figure 20). If we can make this observation deeper at higher- z to study the earlier stage of

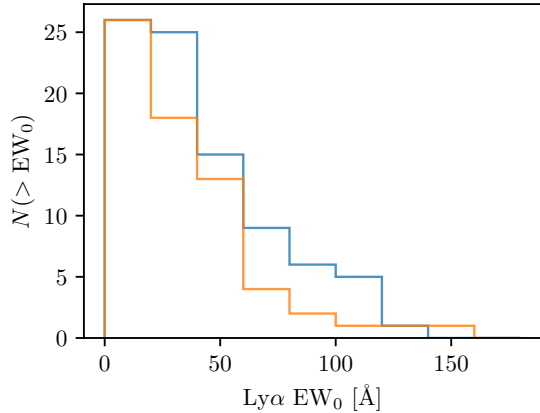


Figure 21. The difference in the Ly α EW distribution of the LAE candidates detected in Y band between the high and low LAE density. The blue (orange) histogram indicates the cumulative EW distribution of the LAEs in the top (bottom) quartile of $n(\text{LAE})/n(\text{LBG})$ at their positions.

reionization, we may be able to detect spatial variation of x_{HI} . However, this is only a validation using this simulation, and other simulations based on different reionization scenarios may give different results, and it is not clear if this is the case in the real universe. Although this simulation model reproduces each observation well in terms of the evolution of the Ly α luminosity function, the auto correlation function, and the Ly α fraction, it may be beyond the scope of this simulation model to reproduce the variance as well. Further investigation of the model is necessary.

5.2. Equivalent Width Distribution

The rest-frame Ly α EW distribution also could be a plausible probe of reionization (Treu et al. 2012, 2013; Jung et al. 2020). We calculate the EW_0 of the LAEs in the same way as Shibuya et al. (2018a). In this analysis, we exclude sources undetected in Y-band, which would cause large uncertainties on the EW_0 measurements. The EW_0 distribution of our LAE sample is similar to Shibuya et al. (2018a). The Kolmogorov-Smirnov test does not find any significant difference between the two distributions (p-value $p = 0.36$). To investigate the relation between the EW_0 and the neutrality, we divide the sample into high and low LAE density regions based on $n(\text{LAE})/n(\text{LBG})$ shown in Figure 14 at the positions of LAEs. When we compare the EW_0 distribution between the top and bottom quartiles of $n(\text{LAE})/n(\text{LBG})$, as shown in Figure 21, the LAEs in the high LAE density region more populate $\text{EW}_0 > 100 \text{ \AA}$, though the statistical significance is not high. We compare the EW_0 distribution with the model prediction of Dijkstra et al. (2011) as shown in Figure 22. While the error bar is large, low $n(\text{LAE})/n(\text{LBG})$ environment might indicate

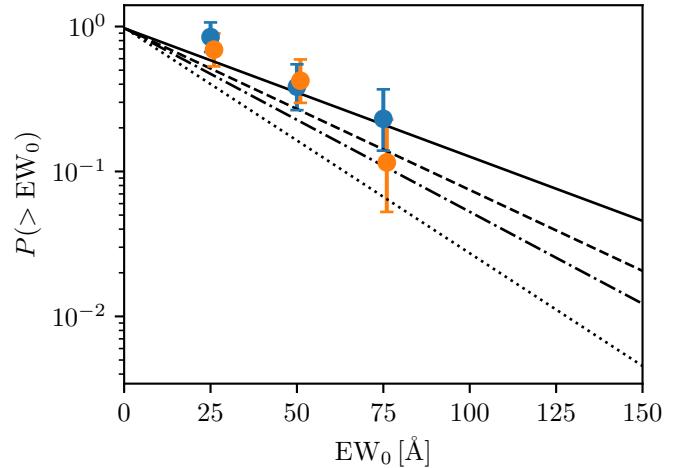


Figure 22. Cumulative probability distribution of EW_0 of the LAEs. Blue (orange) marks indicate the high (low) $n(\text{LAE})/n(\text{LBG})$ environment. Black curves show the model prediction of (Dijkstra et al. 2011) in the universe with $x_{\text{HI}} = 0, 0.23, 0.51,$ and 0.74 from top to bottom.

a high neutral fraction, implying that the LAEs in the highest $n(\text{LAE})/n(\text{LBG})$ environment are surrounded by ionized bubbles. It is in line with the relation that increasing the neutral fraction reduces $n(\text{LAE})/n(\text{LBG})$. While we assume a flat UV continuum when calculating the EW_0 , the uncertainty of the UV slope affects the EW_0 . However, considering the uncertainty is difficult because most of our LAEs are detected only in Y-band redward of the Ly α . The UV slope might depend on the environment, and it will be investigated by future observations.

6. SUMMARY

In this paper, we, for the first time, attempt to quantify the spatially inhomogeneous reionization from the wide-field survey with Subaru HSC.

1. We simultaneously detect 189 LAEs and 179 LBGs at $z \sim 6.6$ in the COSMOS field with large FoV ($\sim 1.5 \text{ deg}^2$) HSC observations. The newly installed filter IB945 makes it possible to detect LBGs at similar redshift to LAEs. The surface number densities of our LAE and LBG samples are consistent with the previous studies.
2. Based on the state-of-the-art simulation of reionization, the observed $n(\text{LAE})/n(\text{LBG}), 0.84^{+0.23}_{-0.27}$, puts a constraint on the average neutral fraction in the FoV as $x_{\text{HI}} < 0.4$, which is consistent with previous studies.
3. By comparing the density distribution of the LAEs and LBGs, we detect a spatial variation over a fac-

tor of three in $n(\text{LAE})/n(\text{LBG})$. Our model predicts that the spatial variation of $n(\text{LAE})/n(\text{LBG})$ corresponds to the spatial variation of the neutral fraction. i.e., the patchy reionization topology. This implies reionization is proceeding in the high LAE density region in our observation, while it is delayed in the low LAE density region.

4. Based on the model, we conclude that the observed large scatter of $n(\text{LAE})/n(\text{LBG})$ can either be explained by the reionization topology or the intrinsic large-scale structure, and it may be difficult to distinguish them with the current survey depth.
5. LAEs in the high LAE density regions are found to be more populate high EW_0 . The result supports that the observed $n(\text{LAE})/n(\text{LBG})$ is more or less driven by the neutral fraction, though the statistical significance is not high.

ACKNOWLEDGMENTS

T. Y. is supported by International Graduate Program for Excellence in Earth-Space Science (IGPEES). N. K. is supported by JSPS grant 21H04490. A. K. I. is supported by JSPS grant 21H04489. K. I. acknowledges support from JSPS grant 20J12461. R. M. acknowledges a Japan Society for the Promotion of Science (JSPS) Fellowship at Japan and the JSPS KAKENHI grant No. JP18J40088.

This paper is based on data collected at the Subaru Telescope and retrieved from the HSC data archive system, which is operated by Subaru Telescope and Astronomy Data Center (ADC) at NAOJ. Data analysis was in part carried out with the cooperation of Center for Computational Astrophysics (CfCA) at NAOJ. We are honored and grateful for the opportunity of observing the Universe from Maunakea, which has the cultural, historical and natural significance in Hawaii.

The Hyper Suprime-Cam (HSC) collaboration includes the astronomical communities of Japan and Taiwan, and Princeton University. The HSC instrumentation and software were developed by the National Astronomical Observatory of Japan (NAOJ), the Kavli Institute for the Physics and Mathematics of the Universe (Kavli IPMU), the University of Tokyo, the High

Energy Accelerator Research Organization (KEK), the Academia Sinica Institute for Astronomy and Astrophysics in Taiwan (ASIAA), and Princeton University. Funding was contributed by the FIRST program from the Japanese Cabinet Office, the Ministry of Education, Culture, Sports, Science and Technology (MEXT), the Japan Society for the Promotion of Science (JSPS), Japan Science and Technology Agency (JST), the Toray Science Foundation, NAOJ, Kavli IPMU, KEK, ASIAA, and Princeton University.

This paper makes use of software developed for Vera C. Rubin Observatory. We thank the Rubin Observatory for making their code available as free software at <http://pipelines.lsst.io/>.

The Pan-STARRS1 Surveys (PS1) and the PS1 public science archive have been made possible through contributions by the Institute for Astronomy, the University of Hawaii, the Pan-STARRS Project Office, the Max Planck Society and its participating institutes, the Max Planck Institute for Astronomy, Heidelberg, and the Max Planck Institute for Extraterrestrial Physics, Garching, The Johns Hopkins University, Durham University, the University of Edinburgh, the Queen's University Belfast, the Harvard-Smithsonian Center for Astrophysics, the Las Cumbres Observatory Global Telescope Network Incorporated, the National Central University of Taiwan, the Space Telescope Science Institute, the National Aeronautics and Space Administration under grant No. NNX08AR22G issued through the Planetary Science Division of the NASA Science Mission Directorate, the National Science Foundation grant No. AST-1238877, the University of Maryland, Eotvos Lorand University (ELTE), the Los Alamos National Laboratory, and the Gordon and Betty Moore Foundation.

This research has made use of NASA's Astrophysics Data System.

Software: `adstex` (<https://github.com/yymao/adstex>), `Astropy` (Astropy Collaboration et al. 2013, 2018), `Datashader` (<https://datashader.org/>), `Jupyter` (Kluyver et al. 2016), `Matplotlib` (Hunter 2007), `Numpy` (Harris et al. 2020), `pandas` (Reback et al. 2021; McKinney 2010), `SciPy` (Virtanen et al. 2020), `uncertainties` (<http://pythonhosted.org/uncertainties/>)

REFERENCES

- Aihara, H., Arimoto, N., Armstrong, R., et al. 2018a, PASJ, 70, S4, doi: 10.1093/pasj/psx066
- Aihara, H., Armstrong, R., Bickerton, S., et al. 2018b, PASJ, 70, S8, doi: 10.1093/pasj/psx081

- Aihara, H., AlSayyad, Y., Ando, M., et al. 2019, PASJ, 71, 114, doi: [10.1093/pasj/psz103](https://doi.org/10.1093/pasj/psz103)
- Astropy Collaboration, Robitaille, T. P., Tollerud, E. J., et al. 2013, A&A, 558, A33, doi: [10.1051/0004-6361/201322068](https://doi.org/10.1051/0004-6361/201322068)
- Astropy Collaboration, Price-Whelan, A. M., Sipőcz, B. M., et al. 2018, AJ, 156, 123, doi: [10.3847/1538-3881/aabc4f](https://doi.org/10.3847/1538-3881/aabc4f)
- Becker, G. D., Bolton, J. S., Madau, P., et al. 2015, MNRAS, 447, 3402, doi: [10.1093/mnras/stu2646](https://doi.org/10.1093/mnras/stu2646)
- Bertin, E. 2011, in *Astronomical Society of the Pacific Conference Series*, Vol. 442, *Astronomical Data Analysis Software and Systems XX*, ed. I. N. Evans, A. Accomazzi, D. J. Mink, & A. H. Rots, 435
- Bertin, E., & Arnouts, S. 1996, A&AS, 117, 393, doi: [10.1051/aas:1996164](https://doi.org/10.1051/aas:1996164)
- Boquien, M., Burgarella, D., Roehlly, Y., et al. 2019, A&A, 622, A103, doi: [10.1051/0004-6361/201834156](https://doi.org/10.1051/0004-6361/201834156)
- Bosch, J., Armstrong, R., Bickerton, S., et al. 2018, PASJ, 70, S5, doi: [10.1093/pasj/psx080](https://doi.org/10.1093/pasj/psx080)
- Bosch, J., AlSayyad, Y., Armstrong, R., et al. 2019, in *Astronomical Society of the Pacific Conference Series*, Vol. 523, *Astronomical Data Analysis Software and Systems XXVII*, ed. P. J. Teuben, M. W. Pound, B. A. Thomas, & E. M. Warner, 521. <https://arxiv.org/abs/1812.03248>
- Bosman, S. E. I., Fan, X., Jiang, L., et al. 2018, MNRAS, 479, 1055, doi: [10.1093/mnras/sty1344](https://doi.org/10.1093/mnras/sty1344)
- Bouwens, R. J., Illingworth, G. D., Oesch, P. A., et al. 2015, ApJ, 803, 34, doi: [10.1088/0004-637X/803/1/34](https://doi.org/10.1088/0004-637X/803/1/34)
- Bruzual, G., & Charlot, S. 2003, MNRAS, 344, 1000, doi: [10.1046/j.1365-8711.2003.06897.x](https://doi.org/10.1046/j.1365-8711.2003.06897.x)
- Calzetti, D., Armus, L., Bohlin, R. C., et al. 2000, ApJ, 533, 682, doi: [10.1086/308692](https://doi.org/10.1086/308692)
- Cassata, P., Tasca, L. A. M., Le Fèvre, O., et al. 2015, A&A, 573, A24, doi: [10.1051/0004-6361/201423824](https://doi.org/10.1051/0004-6361/201423824)
- Castellano, M., Pentericci, L., Vanzella, E., et al. 2018, ApJL, 863, L3, doi: [10.3847/2041-8213/aad59b](https://doi.org/10.3847/2041-8213/aad59b)
- Chambers, K. C., Magnier, E. A., Metcalfe, N., et al. 2016, arXiv e-prints, arXiv:1612.05560. <https://arxiv.org/abs/1612.05560>
- Chartab, N., Mobasher, B., Darvish, B., et al. 2020, ApJ, 890, 7, doi: [10.3847/1538-4357/ab61fd](https://doi.org/10.3847/1538-4357/ab61fd)
- Coleman, G. D., Wu, C. C., & Weedman, D. W. 1980, ApJS, 43, 393, doi: [10.1086/190674](https://doi.org/10.1086/190674)
- Coupon, J., Czakon, N., Bosch, J., et al. 2018, PASJ, 70, S7, doi: [10.1093/pasj/psx047](https://doi.org/10.1093/pasj/psx047)
- Curtis-Lake, E., McLure, R. J., Pearce, H. J., et al. 2012, MNRAS, 422, 1425, doi: [10.1111/j.1365-2966.2012.20720.x](https://doi.org/10.1111/j.1365-2966.2012.20720.x)
- Dijkstra, M., Mesinger, A., & Wyithe, J. S. B. 2011, MNRAS, 414, 2139, doi: [10.1111/j.1365-2966.2011.18530.x](https://doi.org/10.1111/j.1365-2966.2011.18530.x)
- Fan, X., Strauss, M. A., Becker, R. H., et al. 2006, AJ, 132, 117, doi: [10.1086/504836](https://doi.org/10.1086/504836)
- Finkelstein, S. L., D'Aloisio, A., Paardekooper, J.-P., et al. 2019, ApJ, 879, 36, doi: [10.3847/1538-4357/ab1ea8](https://doi.org/10.3847/1538-4357/ab1ea8)
- Fumagalli, M., Patel, S. G., Franx, M., et al. 2012, ApJL, 757, L22, doi: [10.1088/2041-8205/757/2/L22](https://doi.org/10.1088/2041-8205/757/2/L22)
- Furusawa, H., Koike, M., Takata, T., et al. 2018, PASJ, 70, S3, doi: [10.1093/pasj/psx079](https://doi.org/10.1093/pasj/psx079)
- Gunn, J. E., & Stryker, L. L. 1983, ApJS, 52, 121, doi: [10.1086/190861](https://doi.org/10.1086/190861)
- HALL, P. 1982, Biometrika, 69, 383, doi: [10.1093/biomet/69.2.383](https://doi.org/10.1093/biomet/69.2.383)
- Harikane, Y., Ono, Y., Ouchi, M., et al. 2021, arXiv e-prints, arXiv:2108.01090. <https://arxiv.org/abs/2108.01090>
- Harris, C. R., Millman, K. J., van der Walt, S. J., et al. 2020, Nature, 585, 357, doi: [10.1038/s41586-020-2649-2](https://doi.org/10.1038/s41586-020-2649-2)
- Higuchi, R., Ouchi, M., Ono, Y., et al. 2019, ApJ, 879, 28, doi: [10.3847/1538-4357/ab2192](https://doi.org/10.3847/1538-4357/ab2192)
- Hoag, A., Bradač, M., Huang, K., et al. 2019, ApJ, 878, 12, doi: [10.3847/1538-4357/ab1de7](https://doi.org/10.3847/1538-4357/ab1de7)
- Hu, W., Wang, J., Infante, L., et al. 2021, Nature Astronomy, 5, 485, doi: [10.1038/s41550-020-01291-y](https://doi.org/10.1038/s41550-020-01291-y)
- Hunter, J. D. 2007, Computing in Science and Engineering, 9, 90, doi: [10.1109/MCSE.2007.55](https://doi.org/10.1109/MCSE.2007.55)
- Inoue, A. K., Hasegawa, K., Ishiyama, T., et al. 2018, PASJ, 70, 55, doi: [10.1093/pasj/psy048](https://doi.org/10.1093/pasj/psy048)
- Inoue, A. K., Yamanaka, S., Ouchi, M., et al. 2020, PASJ, 72, 101, doi: [10.1093/pasj/psaa100](https://doi.org/10.1093/pasj/psaa100)
- Ivezić, Ž., Kahn, S. M., Tyson, J. A., et al. 2019, ApJ, 873, 111, doi: [10.3847/1538-4357/ab042c](https://doi.org/10.3847/1538-4357/ab042c)
- Jones, M. C. 1993, Statistics and Computing, 3, 135, doi: [10.1007/bf00147776](https://doi.org/10.1007/bf00147776)
- Jung, I., Finkelstein, S. L., Dickinson, M., et al. 2020, ApJ, 904, 144, doi: [10.3847/1538-4357/abbd44](https://doi.org/10.3847/1538-4357/abbd44)
- Jurić, M., Kantor, J., Lim, K. T., et al. 2017, in *Astronomical Society of the Pacific Conference Series*, Vol. 512, *Astronomical Data Analysis Software and Systems XXV*, ed. N. P. F. Lorente, K. Shortridge, & R. Wayth, 279. <https://arxiv.org/abs/1512.07914>
- Kawanomoto, S., Uruguchi, F., Komiyama, Y., et al. 2018, PASJ, 70, 66, doi: [10.1093/pasj/psy056](https://doi.org/10.1093/pasj/psy056)
- Khostovan, A. A., Sobral, D., Mobasher, B., et al. 2016, MNRAS, 463, 2363, doi: [10.1093/mnras/stw2174](https://doi.org/10.1093/mnras/stw2174)
- Kluyver, T., Benjamin, R.-K., Fernando, P., et al. 2016, Stand Alone, 0, 87–90, doi: [10.3233/978-1-61499-649-1-87](https://doi.org/10.3233/978-1-61499-649-1-87)

- Knapp, G. R., Leggett, S. K., Fan, X., et al. 2004, *AJ*, 127, 3553, doi: [10.1086/420707](https://doi.org/10.1086/420707)
- Komiyama, Y., Obuchi, Y., Nakaya, H., et al. 2018, *PASJ*, 70, S2, doi: [10.1093/pasj/psx069](https://doi.org/10.1093/pasj/psx069)
- Madau, P. 1995, *ApJ*, 441, 18, doi: [10.1086/175332](https://doi.org/10.1086/175332)
- Magnier, E. A., Schlafly, E., Finkbeiner, D., et al. 2013, *ApJS*, 205, 20, doi: [10.1088/0067-0049/205/2/20](https://doi.org/10.1088/0067-0049/205/2/20)
- Mason, C. A., Fontana, A., Treu, T., et al. 2019, *MNRAS*, 485, 3947, doi: [10.1093/mnras/stz632](https://doi.org/10.1093/mnras/stz632)
- McKinney, W. 2010, in *Proceedings of the 9th Python in Science Conference (SciPy)*, doi: [10.25080/majora-92bf1922-00a](https://doi.org/10.25080/majora-92bf1922-00a)
- McQuinn, M. 2016, *ARA&A*, 54, 313, doi: [10.1146/annurev-astro-082214-122355](https://doi.org/10.1146/annurev-astro-082214-122355)
- Meiksin, A. 2006, *MNRAS*, 365, 807, doi: [10.1111/j.1365-2966.2005.09756.x](https://doi.org/10.1111/j.1365-2966.2005.09756.x)
- Meyer, R. A., Kakiichi, K., Bosman, S. E. I., et al. 2020, *MNRAS*, 494, 1560, doi: [10.1093/mnras/staa746](https://doi.org/10.1093/mnras/staa746)
- Miyazaki, S., Komiyama, Y., Kawanomoto, S., et al. 2018, *PASJ*, 70, S1, doi: [10.1093/pasj/psx063](https://doi.org/10.1093/pasj/psx063)
- Naidu, R. P., Tacchella, S., Mason, C. A., et al. 2020, *ApJ*, 892, 109, doi: [10.3847/1538-4357/ab7cc9](https://doi.org/10.3847/1538-4357/ab7cc9)
- Oke, J. B., & Gunn, J. E. 1983, *ApJ*, 266, 713, doi: [10.1086/160817](https://doi.org/10.1086/160817)
- Ono, Y., Ouchi, M., Mobasher, B., et al. 2012, *ApJ*, 744, 83, doi: [10.1088/0004-637X/744/2/83](https://doi.org/10.1088/0004-637X/744/2/83)
- Ono, Y., Ouchi, M., Harikane, Y., et al. 2018, *PASJ*, 70, S10, doi: [10.1093/pasj/psx103](https://doi.org/10.1093/pasj/psx103)
- Ono, Y., Itoh, R., Shibuya, T., et al. 2021, *ApJ*, 911, 78, doi: [10.3847/1538-4357/abea15](https://doi.org/10.3847/1538-4357/abea15)
- Ouchi, M., Ono, Y., & Shibuya, T. 2020, *ARA&A*, 58, 617, doi: [10.1146/annurev-astro-032620-021859](https://doi.org/10.1146/annurev-astro-032620-021859)
- Ouchi, M., Shimasaku, K., Furusawa, H., et al. 2010, *ApJ*, 723, 869, doi: [10.1088/0004-637X/723/1/869](https://doi.org/10.1088/0004-637X/723/1/869)
- Ouchi, M., Harikane, Y., Shibuya, T., et al. 2018, *PASJ*, 70, S13, doi: [10.1093/pasj/psx074](https://doi.org/10.1093/pasj/psx074)
- Planck Collaboration, Aghanim, N., Akrami, Y., et al. 2020, *A&A*, 641, A6, doi: [10.1051/0004-6361/201833910](https://doi.org/10.1051/0004-6361/201833910)
- Reback, J., Jbrockmendel, McKinney, W., et al. 2021, *pandas-dev/pandas: Pandas 1.3.0, v1.3.0, Zenodo*, doi: [10.5281/zenodo.3509134](https://doi.org/10.5281/zenodo.3509134)
- Reddy, N. A., Shapley, A. E., Sanders, R. L., et al. 2018, *ApJ*, 869, 92, doi: [10.3847/1538-4357/aaed1e](https://doi.org/10.3847/1538-4357/aaed1e)
- Rowe, B. T. P., Jarvis, M., Mandelbaum, R., et al. 2015, *Astronomy and Computing*, 10, 121, doi: [10.1016/j.ascom.2015.02.002](https://doi.org/10.1016/j.ascom.2015.02.002)
- Salpeter, E. E. 1955, *ApJ*, 121, 161, doi: [10.1086/145971](https://doi.org/10.1086/145971)
- Schenker, M. A., Ellis, R. S., Konidakis, N. P., & Stark, D. P. 2014, *ApJ*, 795, 20, doi: [10.1088/0004-637X/795/1/20](https://doi.org/10.1088/0004-637X/795/1/20)
- Schlafly, E. F., Finkbeiner, D. P., Jurić, M., et al. 2012, *ApJ*, 756, 158, doi: [10.1088/0004-637X/756/2/158](https://doi.org/10.1088/0004-637X/756/2/158)
- Shibuya, T., Ouchi, M., & Harikane, Y. 2015, *ApJS*, 219, 15, doi: [10.1088/0067-0049/219/2/15](https://doi.org/10.1088/0067-0049/219/2/15)
- Shibuya, T., Ouchi, M., Harikane, Y., & Nakajima, K. 2019, *ApJ*, 871, 164, doi: [10.3847/1538-4357/aaf64b](https://doi.org/10.3847/1538-4357/aaf64b)
- Shibuya, T., Ouchi, M., Konno, A., et al. 2018a, *PASJ*, 70, S14, doi: [10.1093/pasj/psx122](https://doi.org/10.1093/pasj/psx122)
- Shibuya, T., Ouchi, M., Harikane, Y., et al. 2018b, *PASJ*, 70, S15, doi: [10.1093/pasj/psx107](https://doi.org/10.1093/pasj/psx107)
- Stark, D. P., Ellis, R. S., Chiu, K., Ouchi, M., & Bunker, A. 2010, *MNRAS*, 408, 1628, doi: [10.1111/j.1365-2966.2010.17227.x](https://doi.org/10.1111/j.1365-2966.2010.17227.x)
- Stark, D. P., Ellis, R. S., & Ouchi, M. 2011, *ApJL*, 728, L2, doi: [10.1088/2041-8205/728/1/L2](https://doi.org/10.1088/2041-8205/728/1/L2)
- Suchyta, E., Huff, E. M., Aleksić, J., et al. 2016, *MNRAS*, 457, 786, doi: [10.1093/mnras/stv2953](https://doi.org/10.1093/mnras/stv2953)
- Tilvi, V., Papovich, C., Finkelstein, S. L., et al. 2014, *ApJ*, 794, 5, doi: [10.1088/0004-637X/794/1/5](https://doi.org/10.1088/0004-637X/794/1/5)
- Tilvi, V., Malhotra, S., Rhoads, J. E., et al. 2020, *ApJL*, 891, L10, doi: [10.3847/2041-8213/ab75ec](https://doi.org/10.3847/2041-8213/ab75ec)
- Tonry, J. L., Stubbs, C. W., Lykke, K. R., et al. 2012, *ApJ*, 750, 99, doi: [10.1088/0004-637X/750/2/99](https://doi.org/10.1088/0004-637X/750/2/99)
- Treu, T., Schmidt, K. B., Trenti, M., Bradley, L. D., & Stiavelli, M. 2013, *ApJL*, 775, L29, doi: [10.1088/2041-8205/775/1/L29](https://doi.org/10.1088/2041-8205/775/1/L29)
- Treu, T., Trenti, M., Stiavelli, M., Auger, M. W., & Bradley, L. D. 2012, *ApJ*, 747, 27, doi: [10.1088/0004-637X/747/1/27](https://doi.org/10.1088/0004-637X/747/1/27)
- Virtanen, P., Gommers, R., Oliphant, T. E., et al. 2020, *Nature Methods*, 17, 261, doi: [10.1038/s41592-019-0686-2](https://doi.org/10.1038/s41592-019-0686-2)
- Yang, J., Wang, F., Fan, X., et al. 2020, *ApJ*, 904, 26, doi: [10.3847/1538-4357/abbc1b](https://doi.org/10.3847/1538-4357/abbc1b)
- Zhang, H., Ouchi, M., Itoh, R., et al. 2020, *ApJ*, 891, 177, doi: [10.3847/1538-4357/ab7917](https://doi.org/10.3847/1538-4357/ab7917)
- Zheng, Z.-Y., Wang, J., Rhoads, J., et al. 2017, *ApJL*, 842, L22, doi: [10.3847/2041-8213/aa794f](https://doi.org/10.3847/2041-8213/aa794f)

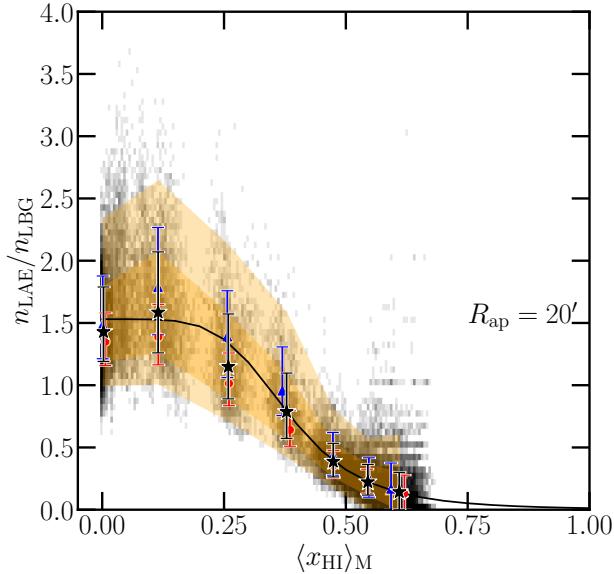


Figure 23. The relation between x_{HI} and $n(\text{LAE})/n(\text{LBG})$ in the simulation data with $\Delta z = 0.1$ top-hat selection function for LAEs and $\Delta z = 0.3$ for LBGs. Colors are the same as Figure 15.

APPENDIX

A. ROBUSTNESS OF THE RELATION BETWEEN $N(\text{LAE})/N(\text{LBG})$ AND X_{HI}

In Section 5.1, we derive the relation between the number ratio $n(\text{LAE})/n(\text{LBG})$ and the neutral fraction x_{HI} using the observed selection functions described in Section 3.3. To see the robustness of the trend, we here make a simpler assumption on the selection function. we use a $\Delta z = 0.1$ top-hat selection function for LAEs and $\Delta z = 0.3$ for LBGs. Figure 23 shows the correlation between x_{HI} and $n(\text{LAE})/n(\text{LBG})$ with this selection. When comparing $n(\text{LAE})/n(\text{LBG})$ between the simulation and observation, we need to correct the difference in selection methods. In the simulation data, we select LAEs and LBGs with the top-hat selection and the photometric selection in the same as the observational data. We use a ratio of the number of the objects with the top-hat selection to that with photometric selection as a correction factor between the simulation and the observation. We derive observed $n(\text{LAE})/n(\text{LBG})$ with the top-hat selection by multiplying the correction factor to the observed number of the objects and derive the neutral fraction in the same way as Section 5.1. The neutral fraction is $x_{\text{HI}} < 0.4$, which is consistent with the result of Section 5.1. We confirm that the effect of the difference in selection methods is negligible and that our results are robust.